A Two-Cool-Season Wind Profiler–Based Analysis of Westward-Directed Gap Flow through the Columbia River Gorge

PAUL J. NEIMAN, DANIEL J. GOTTAS, AND ALLEN B. WHITE

NOAA/Earth System Research Laboratory/Physical Sciences Division, Boulder, Colorado

ABSTRACT

This observational study of westward-directed gap flows through the Columbia River Gorge uses three radar wind profilers during two winter seasons between October 2015 and April 2017, with a focus on the gap-exit region at Troutdale, Oregon. Of the 92 gap-flow events identified at Troutdale, the mean duration was 38.5 h, the mean gap-jet speed was $12 \, m \, s^{-1}$, and the mean gap-flow depth was 570 m MSL. The mean gap-jet height and gap-flow depth were situated below the top of the inner gorge, while a maximum depth of 1087 m MSL was contained within the gorge's outer-wall rim. The mean gap-flow depth was deepest in the cold-air source region east of the gorge and decreased westward to the coast. Strong gap-flow events were longer lived, deeper, and capped by stronger vertical shear than their weak counterparts, and strong (weak) events were forced primarily by a cold-interior anticyclone (offshore cyclone). Deep gap-flow events were longer lived, stronger, and had weaker capping vertical shear than shallow events, and represented a combination of gap-flow and synoptic forcing. Composite temporal analysis shows that gap-flow strength (depth) was maximized midevent (early event), freezing rain was most prevalent during the second half of the event, and accumulated precipitation was greatest late-event. Gap-flow events tended to begin (end) during the evening (morning) hours and were most persistent in January. Surface wind gusts and snow occurrences around Portland, Oregon, were associated primarily with the deepest gap flows, whereas freezing rain occurred predominantly during shallow gap flows.

1. Introduction

The Columbia River Gorge (CRG) is the largest and lowest cross-barrier passage in the Cascade Mountains of Oregon and Washington (Fig. 1), and it is the most prominent location in the region where coastal and continental air masses are channeled through the mountainous terrain as gap flows (e.g., Sharp 2002; Sharp and Mass 2004; Green et al. 2008; Neiman et al. 2018). The CRG is generally <10 km wide below ~700 m MSL and increases in width to ~80 km in the layer between 700 and 2000 m MSL. During the cool season, low pressure dominates offshore and high pressure dominates inland, resulting in the westward extrusion (i.e., easterly gap flow) of cold continental air through the gorge into the normally maritime environment of the populous Portland, Oregon, metropolitan area. Cool-season easterly gap-flow conditions can produce damaging winds in the western gorge and around Portland. Also, reliable winds funneling through the gorge (both westbound and eastbound) make this region ideal for wind energy production (e.g., Wilczak et al. 2019). Easterly gap-flow conditions can also result in snow and freezing rain, as the shallow easterlies undercut moist onshore flow associated with landfalling extratropical cyclones from the Pacific. Adverse impacts on transportation and other societal sectors often ensue.

Previous detailed observational studies of gap flows have revealed complex three-dimensional structures that can evolve rapidly between the gap entrance and exit regions (Mayr et al. 2004; Colle and Mass 2000). In general, deeper and slower flow upstream of the gap accelerates and becomes increasingly shallower across the gap, which culminates in the gap-exit region, where the maximum wind speeds and shallowest depths are observed. Model-simulation studies have shown that both synoptic-scale and mesoscale forcing control these flow behaviors, which include terrain-induced mesoscale effects such as mountain waves, upstream blocking, lee troughing, and surface friction (Gaberšek and Durran 2006; Sharp 2005). For observational measurements to capture these complex flow characteristics adequately, frequent (<3 h) sampling of the vertical structure of

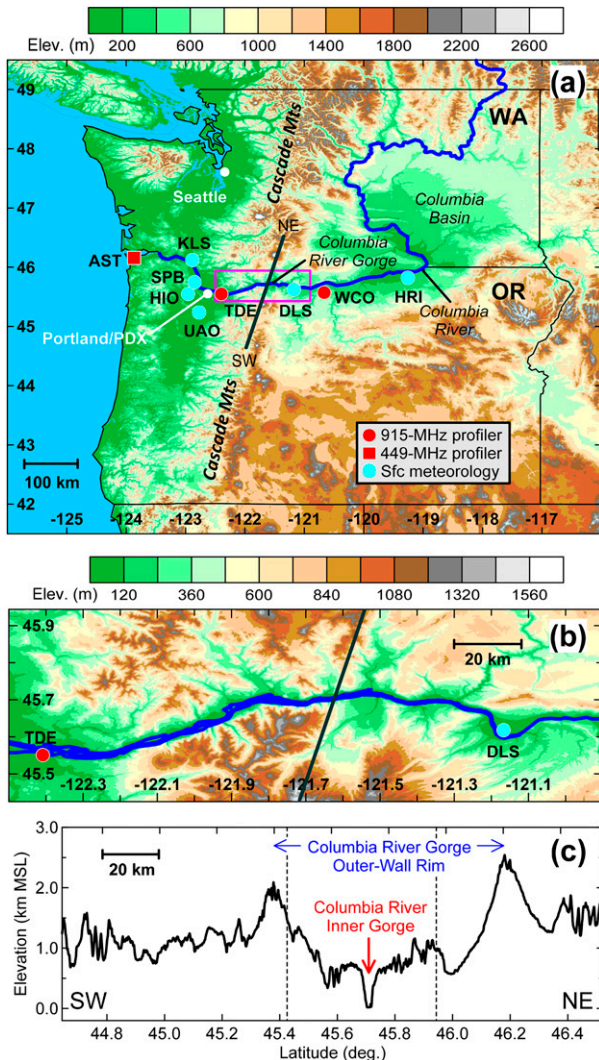*Corresponding author*: Paul J. Neiman, Paul.J.Neiman@noaa.gov

FIG. 1. (a) Terrain base map (m; see color scale above) of Oregon and Washington, showing the locations of the observing sites used in this study: 915-MHz wind profilers at TDE and WCO (red circles), a 449-MHz wind profiler at AST (red square), and surface instrumentation at KLS, SPB, HIO, UAO, DLS, HRI (blue circles), and at PDX (white circle). Surface instruments were also stationed at the wind profiler sites. The Columbia River is marked with a blue line. The pink inset box shows the domain of the zoomed in base map of the Columbia River Gorge region in (b). The dark line NE–SW is a projection for the cross section in (c). (b) Zoomed in terrain base map (m, see color scale above) of the Columbia River Gorge region. The dark line represents the segment of the cross-sectional projection cutting through the domain. (c) Terrain cross section across the Columbia River Gorge along line NE–SW in (a). The vertical dashed lines denote the north and south boundaries in (b).

wind and temperature has been deemed essential at locations both upstream and downstream of the gap (Mayr et al. 2007). Remote sensors, including radar, lidar, and sodar offer potential to fulfill these sampling

requirements and have been used to study the vertical structure of gap-flows in the Birch Creek Valley of Idaho (Finn et al. 2016), the Wipp Valley of Austria (Mayr et al. 2007), the Gastineau Channel of Alaska (Bond et al. 2006), and the Petaluma Gap of California (Neiman et al. 2006). For the observational study of gap flows in the CRG, a radar wind profiler is likely the optimal remote sensor for the following two reasons. First, data-retrieval limitations in weak signal backscattering environments, such as dry continental air within gap flows, are less of an issue when the gap-flow depth is within close range of the radar, as is typically observed in the CRG (e.g., <1.25 km MSL). Second, since precipitation occurs frequently in the CRG, as moist Pacific airstreams overrun the gap flow, signal attenuation prevents data retrieval for both lidar and sodar, whereas ultrahigh-frequency (UHF) radar wind profiler signals are enhanced by precipitation (McDonald et al. 2004) and time–height data coverage is maximized.

Objective analysis of the vertically observed kinematic structure is an effective method for monitoring and studying the complex spatiotemporal characteristics of gap flow. Neiman et al. (2018) established wind speed and directional shear criteria to detect gap flow jet speed and depth for CRG gap flow using individual hourly averaged wind profiles. In this application, these gap flow metrics were used to develop a real-time, web-based, gap-flow detection product that provides situational awareness to forecasters in the National Oceanic and Atmospheric Administration (NOAA) National Weather Service (NWS) Portland Forecast Office. In the new study presented below, these same metrics are utilized to document and study the gap-flow characteristics along the CRG and assess the related meteorological impacts downstream across the Portland metropolitan area.

A thorough literature review of gap flows, both generally and specific to the CRG, is provided in the research-centric contribution by Sharp and Mass (2004) and in the operationally focused study by Neiman et al. (2018). The Sharp and Mass (2004) contribution is the most comprehensive research-oriented observational study to date focusing on cool-season easterly gap flows through the CRG, synoptic controls on these gap flows, and the regional weather and climate impacts of these flows. Although Sharp (2002) and Sharp and Mass (2004) significantly expanded understanding of cool-season gap flows exiting the CRG toward Portland, their observing platforms were limited primarily to monitoring surface conditions, although Sharp (2002) also presented several instantaneous snapshots of gap-flow vertical structure using commercial aircraft and operational radar data.

The present study complements surface observations with unique temporally continuous upper-air data gathered by radar wind profilers during the cool seasons of October 2015–April 2016 and October 2016–April 2017. This dataset provides a comprehensive observational characterization of the composite vertical and temporal structure of gap flows along the Columbia River from the interior basin to the coast, with an emphasis on the exit region of the gorge. Composite wind profiler–based observational metrics of gap flows in the exit region of the CRG—which have not been documented previously in the literature—include the depth of the gap flow and the strength of its jet. We use these metrics to establish their diagnostic relationships with surface wind speed and winter precipitation-type impacts (i.e., snow and freezing rain; rare occurrences of ice pellets excluded) downstream across the Portland metropolitan area. These metrics are also compared to the same metrics generated from an operational rapid-refresh numerical weather prediction model in order to demonstrate a potential application of the gap flow metrics in evaluating model performance.

2. Observing systems and gridded datasets

A suite of research instruments was installed in the CRG and Columbia basin of eastern Oregon and Washington in the fall of 2015 for the second Wind Forecast Improvement Project (WFIP2; Wilczak et al. 2019), an 18-month campaign funded by the U.S. Department of Energy (DOE) and NOAA. Our study utilizes data collected from two key instruments deployed during WFIP2: a NOAA/Earth System Research Laboratory (ESRL) 915-MHz wind profiler at the west end of the CRG at Troutdale, Oregon (TDE) and a second NOAA/ESRL 915-MHz wind profiler in the Columbia basin at Wasco, Oregon (WCO) (Fig. 1, Table 1). Additional instruments used in this study include a 449-MHz wind profiler operated by DOE's Pacific Northwest National Laboratory (PNNL) at the mouth of the Columbia River near Astoria, Oregon (AST), and operational surface meteorology sites along or near the Columbia River at AST; Kelso-Longview, Washington (KLS); Scappoose, OR (SPB); Hillsboro, OR (HIO); Aurora, OR (UAO); PDX; TDE (located 15 km east-southeast of PDX); The Dalles, OR (DLS); and Hermiston, OR (HRI) (Fig. 1, Table 1). These and additional observing platforms are described below.

The 915-MHz wind profilers (e.g., Carter et al. 1995) collected hourly averaged profiles of horizontal wind in high- and low-resolution modes, although we used only the high-resolution mode. Each hourly time stamp is valid at the beginning of the averaging period, and wind

profiles displayed in time–height sections are plotted at the middle of the hour. At TDE, the high-mode profiles extended from 150 to 2523 m MSL with 58-m range-gate spacing. The high-mode profiles at WCO spanned an altitude range of 543–3004 m MSL, also with 58-m resolution. A radio acoustic sounding system (RASS; Martner et al. 1993) accompanied the wind profiler at TDE. The RASS provided hourly profiles of virtual temperature between 150 and 1701 m MSL every 60 m, and they were converted to virtual potential temperature profiles by integrating the hypsometric equation using the surface pressure as a lower boundary and RASS layer-mean virtual temperatures. Gap-flow events with strong winds reduce the RASS vertical coverage to within a couple hundred meters above the radar, thus precluding the opportunity to use RASS in the forthcoming composite analyses. As with the 915-MHz systems, the 449-MHz wind profiler (White et al. 2013) collected data in two modes, with only the high-resolution mode used: 197–5061 m MSL at 101 m intervals.

At each wind profiler site, instruments affixed to a 10-m tower collected the following surface observations every 2 min: pressure, temperature, and relative humidity at 2 m above ground level (AGL) and wind velocity at 10 m AGL. A heated tipping-bucket gauge adjacent to the tower measured precipitation at 2-min intervals. These data were averaged into 1-h blocks. Elsewhere, operational sites at KLS, SPB, PDX, HIO, UAO, DLS, and HRI collected hourly surface pressure, temperature, relative humidity, and wind velocity, as did two additional operational sites at AST and TDE (which are collocated with those wind profilers). Hourly operational reports of precipitation type were provided at TDE, PDX, HIO, UAO, and SPB.

To provide synoptic-scale context for the observational analyses, we utilized the Climate Forecast System Reanalysis (CFSR; Saha et al. 2010) that is available between 1979 and 2011, and the newer, upgraded Climate Forecast System, version 2, operational analysis (CFSv2; Saha et al. 2014) available since 2011. These gridded datasets were developed by NOAA's National Centers for Environmental Prediction (NCEP) and are now maintained by the National Centers for Environmental Information (NCEI). We downloaded these 6-h data from NOAA/NCEI's Operational Model Archive and Distribution System (NOMADS) at $0.5° \times 0.5°$ latitude–longitude resolution and with 64 vertical levels.

3. Composite analysis across two consecutive cool seasons

In this section, we employ composite analysis techniques for the 2015–16 and 2016–17 cool seasons to

TABLE 1. Site information for key observing platforms.

Location	3-letter name	Lat (°N)	Lon (°W)	Elevation (m MSL)	Observing platforms	Agency
Astoria, OR	AST	46.157	123.883	3	449-MHz wind profiler surface meteorology	U.S. DOE/PNNL, NOAA/NWS[a]
Troutdale, OR	TDE	45.554	122.386	12	915-MHz wind profiler RASS disdrometer surface meteorology	NOAA/Earth System Research Laboratory and NOAA/NWS
Portland, OR	PDX	45.596	122.609	6	Surface meteorology	NOAA/NWS
Wasco, OR	WCO	45.590	120.672	462	915-MHz wind profiler surface meteorology	NOAA/Earth System Research Laboratory
Kelso-Longview, WA[a]	KLS	46.117	122.894	6	Surface meteorology	NOAA/NWS
Longview, WA[b]	LOP	46.100	122.950	3	Surface meteorology	NOAA/NWS
Scappoose, OR	SPB	45.769	122.864	17	Surface meteorology	NOAA/NWS
Hillsboro, OR	HIO	45.548	122.956	62	Surface meteorology	NOAA/NWS
Aurora, OR	UAO	45.247	122.771	60	Surface meteorology	NOAA/NWS
The Dalles, OR	DLS	45.619	121.166	72	Surface meteorology	NOAA/NWS
Hermiston, OR	HRI	45.826	119.261	195	Surface meteorology	NOAA/NWS

[a] NWS is the National Weather Service.

[b] At Longview, the sea level pressure at the river site (LOP) was combined with the other surface meteorological variables measured at the airport (KLS), since the pressure sensor at the airport was not working. The combined dataset is referred to as KLS in the body of the paper. Reliable precipitation gauge measurements were not available from either site.

showcase spatiotemporal structural characteristics of gap-flow events observed along the Columbia River corridor from the interior Columbia basin, through the gorge, and westward to the Pacific coast. But before presenting the composite analyses, it is instructive to first examine the vertical-temporal structure and the synoptic environment of a well-defined gap-flow case observed at TDE (Fig. 2). Shallow easterly gap flow persisted for 28 h between 0000 UTC 17 December and 0400 UTC 18 December 2015. The gap-flow depth, ascertained hourly using an automated algorithm (Neiman et al. 2018), was ~400 m MSL at the start of the event, increased to ~800 m during midevent, and decreased to ~250 m by the event's conclusion. The magnitude of the gap flow increased to a maximum value of ~20 m s^{-1} in a jet-like configuration centered at 500 m MSL during the midpoint of the event, when the low-level temperature gradient was enhanced by arctic air over the interior and warm maritime air along the coast in association with an amplified synoptic wave train (Figs. 2c,d). The gap flow strengthened and deepened in conjunction with intensifying maritime south-to-southwesterly flow aloft, as an extratropical cyclone approached the coast (inferred from Figs. 2c,d), and subsequently weakened, eroded, and terminated with the temporal descent of the strong southwesterly airstream toward the surface. Companion RASS observations highlight the cold continental character of the shallow gap flow and the subsequent temporal descent of warmer air toward the surface within the maritime southwesterlies.

a. Vertical and plan-view perspectives

1) FULL 92-CASE WIND PROFILER COMPOSITE RESULTS

To generate composite analyses of gap-flow events, we developed a catalog of events using the observational spectrum of surface and radar wind data at TDE to adapt the event-detection methodology in Neiman et al. (2006) to the CRG. To be labeled as a gap-flow event, the following criteria must be met for six consecutive hours at TDE: 1) surface wind direction of 55°–112°, 2) frictionally rotated layer-mean wind direction of 65°–130° between 100 and 350 m MSL (i.e., in the four lowest wind profiler range gates), and 3) easterly component of ≥5 m s^{-1} in the same 100–350 m layer. Of note, the broad wind direction range in the 100–350 m MSL layer is needed to capture backing or veering wind profiles, while surface-wind speed criteria are excluded due to the frequent flow-decoupling influences of local drainage flows from the Sandy River located southeast of TDE. Collectively, the average wind direction of 90° corresponds to the CRG orientation. Between 28 September 2015 and 30 June 2017, 100 gap-flow events were observed exiting the CRG. For the cool-season period October–April, when cold air in the interior and precipitation are most likely, 92 cases spanning 3546 h were observed (Table 2), with 44 occurring during year 1 (i.e., October 2015–April 2016) and 48 during year 2 (i.e., October 2016–April 2017).
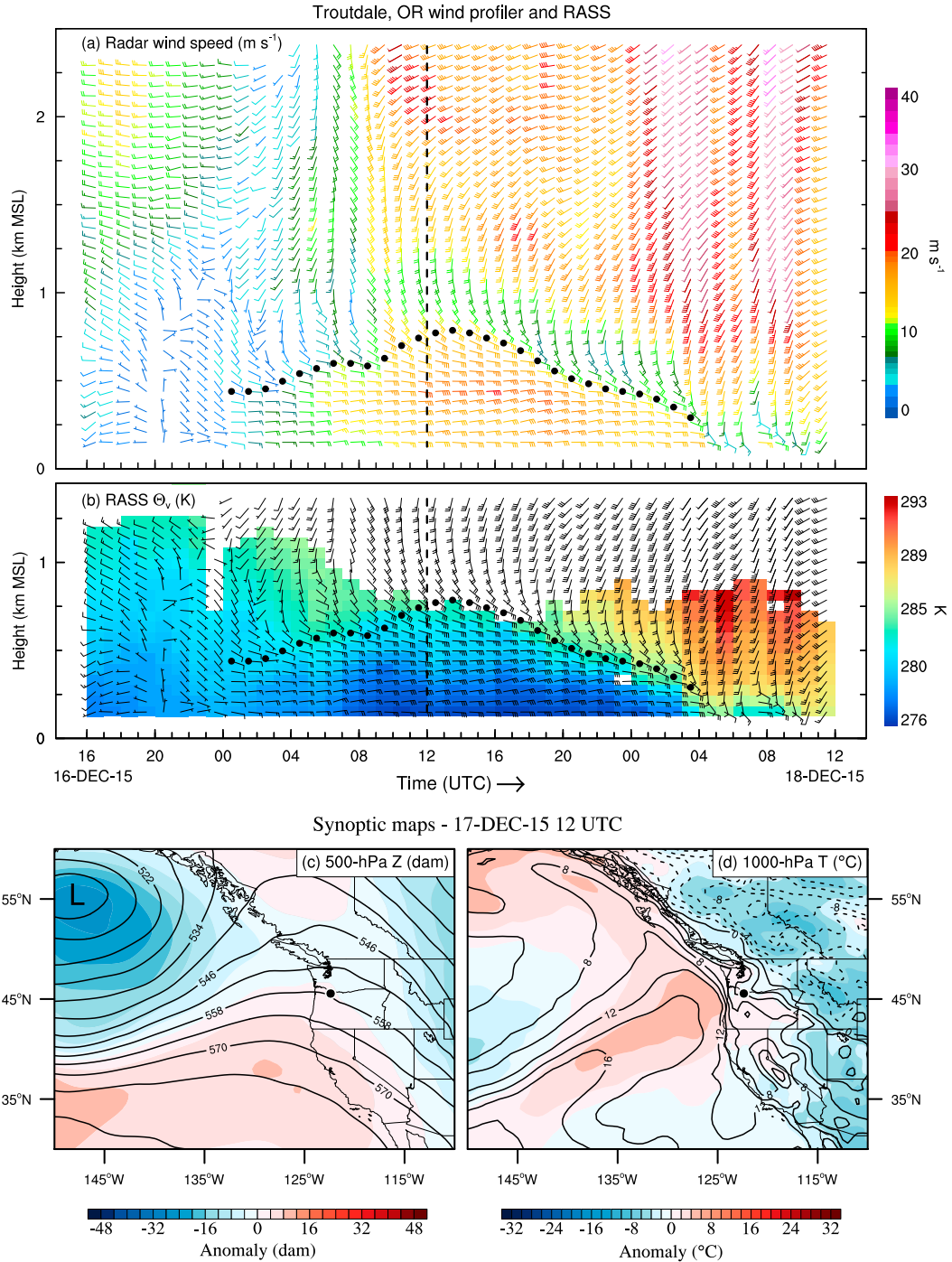
Troutdale, OR wind profiler and RASS

FIG. 2. Time–height sections of data from the 915-MHz wind profiler and RASS at Troutdale, Oregon (TDE), between 1600 UTC 16 Dec and 1200 UTC 18 Dec 2015, and accompanying plan-view synoptic maps at 1200 UTC 17 Dec 2015 derived from NOAA's Climate Forecast System: (a) Hourly radar wind profiles (flag: $25\,\mathrm{m\,s^{-1}}$; barb: $5\,\mathrm{m\,s^{-1}}$; half-barb: $2.5\,\mathrm{m\,s^{-1}}$) color-coded by wind speed ($\mathrm{m\,s^{-1}}$), and the top of the gap flow (black dots) derived from the algorithm of Neiman et al. (2018); (b) hourly color-coded profiles of RASS virtual potential temperature (θ_v; K), and black dots are as in (a); (c) analysis and anomaly (solid and color-filled contours, respectively) for 500-hPa height (dam); and (d) as in (c), but for 1000-hPa temperature (°C). The vertical black dashed lines in (a) and (b) represent the time of the analyses in (c) and (d).

TABLE 2. Gap flow case inventory and mean gap-jet characteristics measured by the Troutdale, Oregon, wind profiler, and collocated precipitation, during the two cool seasons of October 2015–April 2016 and October 2016–April 2017. The three cases highlighted in bold font are described in detail in section 4 because they produced notable impacts across the Portland metropolitan area.

Start date/time	End date/time	Gap flow event (No. of h)	Gap flow jet: Altitude of max easterly flow (m, MSL)	Gap flow jet: Magnitude of max easterly flow (m s⁻¹)	Gap flow jet: Wind direction in max easterly flow (°)	Gap flow depth (m, MSL)	Zonal vertical wind shear atop the gap flow (m s⁻¹ km⁻¹)	Precipitation (mm)
2100 UTC 4 Oct 2015	1200 UTC 6 Oct 2015	39	610	11.4	84.0	805	20.2	0.000
0000 UTC 9 Oct 2015	1700 UTC 9 Oct 2015	17	303	9.4	87.9	454	28.7	0.000
0500 UTC 15 Oct 2015	2200 UTC 16 Oct 2015	41	675	14.9	83.0	900	25.0	0.000
1500 UTC 24 Oct 2015	2300 UTC 25 Oct 2015	32	424	14.5	84.6	667	33.6	11.176
0500 UTC 27 Oct 2015	1800 UTC 28 Oct 2015	37	439	11.0	84.0	633	25.4	3.302
0800 UTC 19 Nov 2015	1900 UTC 19 Nov 2015	11	375	10.5	80.0	590	29.8	10.160
1400 UTC 20 Nov 2015	1800 UTC 23 Nov 2015	76	523	15.9	81.9	741	31.8	0.000
1400 UTC 26 Nov 2015	0100 UTC 4 Dec 2015	179	494	17.5	88.6	701	44.4	17.780
0600 UTC 5 Dec 2015	1200 UTC 6 Dec 2015	30	170	13.6	95.8	419	26.2	7.366
0500 UTC 7 Dec 2015	1900 UTC 7 Dec 2015	14	150	9.5	90.2	364	32.4	78.232
0100 UTC 10 Dec 2015	1000 UTC 10 Dec 2015	9	368	12.2	99.3	581	22.1	1.778
1400 UTC 11 Dec 2015	0300 UTC 12 Dec 2015	13	285	10.4	92.3	478	18.8	13.970
0000 UTC 17 Dec 2015	0400 UTC 18 Dec 2015	28	347	14.9	87.2	572	35.8	35.560
1400 UTC 26 Dec 2015	1200 UTC 28 Dec 2015	46	386	11.8	90.0	571	35.2	2.794
1200 UTC 29 Dec 2015	2200 UTC 7 Jan 2016	226	475	16.6	88.1	709	34.0	9.398
1800 UTC 8 Jan 2016	1700 UTC 13 Jan 2016	119	366	15.3	89.8	582	38.8	25.654
1600 UTC 14 Jan 2016	1000 UTC 15 Jan 2016	18	298	10.1	88.2	490	23.6	3.048
2200 UTC 15 Jan 2016	1700 UTC 16 Jan 2016	19	233	12.5	89.9	446	28.0	7.112
0600 UTC 17 Jan 2016	0000 UTC 18 Jan 2016	18	233	13.7	94.1	457	28.9	19.558
1700 UTC 18 Jan 2016	2300 UTC 19 Jan 2016	30	214	9.8	91.2	424	24.3	12.700
2000 UTC 20 Jan 2016	1300 UTC 22 Jan 2016	41	314	15.1	101.0	560	49.8	12.954
0100 UTC 23 Jan 2016	1000 UTC 23 Jan 2016	9	478	12.8	84.8	751	8.9	1.016
0500 UTC 25 Jan 2016	1400 UTC 28 Jan 2016	81	214	10.6	91.3	415	35.1	10.922
0800 UTC 29 Jan 2016	1700 UTC 29 Jan 2016	9	236	9.2	94.9	504	10.8	4.064
0700 UTC 3 Feb 2016	0100 UTC 4 Feb 2016	18	208	11.3	92.7	387	24.8	3.302
0400 UTC 5 Feb 2016	2100 UTC 5 Feb 2016	17	251	10.2	93.6	464	35.1	0.000
1200 UTC 7 Feb 2016	1700 UTC 10 Feb 2016	77	407	17.0	86.7	633	45.4	0.000
0800 UTC 11 Feb 2016	2000 UTC 12 Feb 2016	36	385	12.6	90.2	563	35.7	8.382
0200 UTC 17 Feb 2016	0000 UTC 18 Feb 2016	22	436	12.7	84.0	615	29.1	0.254
1000 UTC 19 Feb 2016	1800 UTC 19 Feb 2016	8	244	10.2	96.4	424	19.5	1.778
0100 UTC 21 Feb 2016	1800 UTC 21 Feb 2016	17	456	13.2	88.1	695	20.2	0.000
0500 UTC 23 Feb 2016	2100 UTC 26 Feb 2016	88	458	13.7	86.8	660	37.0	0.000
0400 UTC 28 Feb 2016	1400 UTC 28 Feb 2016	10	176	10.6	94.4	394	35.7	0.000
0300 UTC 1 Mar 2016	2000 UTC 1 Mar 2016	17	208	12.2	93.9	426	33.0	13.970
1600 UTC 2 Mar 2016	0600 UTC 3 Mar 2016	14	323	10.9	88.8	530	26.2	6.350
0300 UTC 4 Mar 2016	0800 UTC 5 Mar 2016	29	202	9.8	90.3	421	31.5	0.000

TABLE 2. (Continued)

Start date/time	End date/time	Gap flow event (No. of h)	Gap flow jet: Altitude of max easterly flow (m, MSL)	Gap flow jet: Magnitude of max easterly flow (m s⁻¹)	Gap flow jet: Wind direction in max easterly flow (°)	Gap flow depth (m, MSL)	Zonal vertical wind shear atop the gap flow (m s⁻¹ km⁻¹)	Precipitation (mm)
2000 UTC 5 Mar 2016	0400 UTC 6 Mar 2016	8	396	11.2	92.8	557	6.8	4.826
1100 UTC 9 Mar 2016	0800 UTC 10 Mar 2016	21	243	14.2	96.4	434	32.7	14.224
0300 UTC 11 Mar 2016	0300 UTC 12 Mar 2016	24	333	12.5	91.0	549	18.8	2.286
1000 UTC 13 Mar 2016	1700 UTC 13 Mar 2016	7	158	10.9	92.9	404	18.7	8.128
1700 UTC 17 Mar 2016	2200 UTC 20 Mar 2016	77	635	14.2	88.6	837	19.0	3.048
0800 UTC 26 Mar 2016	1800 UTC 26 Mar 2016	10	352	6.1	83.5	469	20.2	0.000
0500 UTC 7 Apr 2016	1200 UTC 8 Apr 2016	31	607	13.8	80.4	837	17.5	0.000
0400 UTC 17 Apr 2016	1600 UTC 19 Apr 2016	60	575	12.8	83.1	817	15.5	0.000
1300 UTC 11 Oct 2016	0400 UTC 14 Oct 2016	63	392	12.2	88.6	577	33.9	44.704
1300 UTC 15 Oct 2016	2000 UTC 15 Oct 2016	7	207	12.0	97.6	379	13.7	8.636
1300 UTC 19 Oct 2016	1200 UTC 20 Oct 2016	23	253	8.4	90.7	421	28.1	5.842
1500 UTC 22 Oct 2016	1600 UTC 24 Oct 2016	49	352	10.6	89.6	551	23.0	2.794
0200 UTC 26 Oct 2016	0000 UTC 27 Oct 2016	22	360	12.1	95.4	537	22.4	16.256
0900 UTC 28 Oct 2016	1600 UTC 29 Oct 2016	31	389	11.3	88.6	630	19.8	7.366
0100 UTC 30 Oct 2016	0100 UTC 31 Oct 2016	24	444	12.9	86.8	663	20.3	2.286
0600 UTC 2 Nov 2016	0200 UTC 3 Nov 2016	20	235	8.4	88.1	399	28.2	0.254
0000 UTC 4 Nov 2016	1500 UTC 5 Nov 2016	39	317	12.0	91.5	506	32.9	0.000
0200 UTC 7 Nov 2016	0500 UTC 9 Nov 2016	51	363	11.9	88.1	554	32.2	0.000
0300 UTC 10 Nov 2016	0700 UTC 12 Nov 2016	52	433	12.9	84.4	664	29.9	0.000
2300 UTC 14 Nov 2016	0800 UTC 15 Nov 2016	9	176	8.2	89.8	394	22.6	26.162
0100 UTC 18 Nov 2016	1900 UTC 20 Nov 2016	66	390	14.4	94.5	610	23.5	2.286
1000 UTC 22 Nov 2016	0300 UTC 23 Nov 2016	17	245	10.3	95.7	430	26.3	8.382
1400 UTC 25 Nov 2016	1800 UTC 26 Nov 2016	28	234	10.3	95.2	445	29.5	2.540
0500 UTC 7 Dec 2016	**1400 UTC 10 Dec 2016**	**81**	**462**	**16.4**	**85.0**	**678**	**29.9**	**16.256**
0600 UTC 13 Dec 2016	1900 UTC 16 Dec 2016	85	617	13.0	78.7	809	21.3	0.000
0300 UTC 17 Dec 2016	1200 UTC 17 Dec 2016	9	201	7.6	91.8	439	20.7	0.000
0100 UTC 19 Dec 2016	0800 UTC 19 Dec 2016	7	166	9.3	92.9	383	32.6	0.000
0000 UTC 22 Dec 2016	1500 UTC 23 Dec 2016	39	323	10.8	91.5	544	30.5	1.270
0200 UTC 26 Dec 2016	0100 UTC 27 Dec 2016	23	153	7.8	97.9	335	19.8	0.000
0100 UTC 29 Dec 2016	1700 UTC 29 Dec 2016	16	425	11.0	85.6	625	31.8	0.000
0300 UTC 2 Jan 2017	0600 UTC 5 Jan 2017	75	953	18.7	89.5	1087	12.1	0.000
1000 UTC 5 Jan 2017	0500 UTC 9 Jan 2017	91	432	17.2	87.1	675	42.1	12.700
0300 UTC 10 Jan 2017	**0300 UTC 19 Jan 2017**	**216**	**365**	**17.0**	**86.8**	**603**	**42.4**	**32.004**
0400 UTC 20 Jan 2017	2300 UTC 21 Jan 2017	43	284	11.8	90.2	528	25.6	7.112
0500 UTC 22 Jan 2017	1500 UTC 22 Jan 2017	10	352	13.7	92.2	520	19.0	1.524
0100 UTC 23 Jan 2017	1900 UTC 23 Jan 2017	18	240	10.3	86.9	474	25.0	0.000
0500 UTC 27 Jan 2017	1900 UTC 29 Jan 2017	62	327	14.5	87.6	557	50.0	0.000
2300 UTC 31 Jan 2017	**0500 UTC 5 Feb 2017**	**78**	**697**	**19.7**	**88.1**	**876**	**26.6**	**7.366**
0900 UTC 7 Feb 2017	1900 UTC 9 Feb 2017	58	338	12.8	87.4	548	33.2	19.812

TABLE 2. (*Continued*)

Start date/time	End date/time	Gap flow event (No. of h)	Gap flow jet: Altitude of max easterly flow (m, MSL)	Gap flow jet: Magnitude of max easterly flow (m s⁻¹)	Gap flow jet: Wind direction in max easterly flow (°)	Gap flow depth (m, MSL)	Zonal vertical wind shear atop the gap flow (m s⁻¹ km⁻¹)	Precipitation (mm)
0500 UTC 12 Feb 2017	0900 UTC 16 Feb 2017	100	431	16.9	86.0	656	35.1	10.668
1300 UTC 17 Feb 2017	1800 UTC 18 Feb 2017	29	574	10.2	79.1	757	12.4	0.762
0800 UTC 20 Feb 2017	1800 UTC 20 Feb 2017	10	294	9.7	82.2	545	19.3	13.462
0500 UTC 25 Feb 2017	1400 UTC 25 Feb 2017	9	497	5.2	74.8	684	11.6	0.000
0800 UTC 11 Mar 2017	1400 UTC 11 Mar 2017	6	381	8.4	86.0	495	32.1	0.000
0300 UTC 13 Mar 2017	1900 UTC 13 Mar 2017	16	150	7.8	97.5	364	23.0	2.032
0500 UTC 17 Mar 2017	1100 UTC 18 Mar 2017	30	306	10.8	94.6	526	32.6	5.588
0300 UTC 20 Mar 2017	0800 UTC 22 Mar 2017	53	479	14.7	89.5	718	27.8	12.446
0500 UTC 24 Mar 2017	1300 UTC 24 Mar 2017	8	200	9.5	96.5	403	16.8	10.160
1600 UTC 26 Mar 2017	0100 UTC 27 Mar 2017	9	227	8.7	94.7	452	18.2	7.366
0600 UTC 4 Apr 2017	1700 UTC 5 Apr 2017	35	299	10.1	90.2	512	24.1	0.254
0200 UTC 7 Apr 2017	0900 UTC 7 Apr 2017	7	530	11.1	99.9	739	1.8	1.270
0900 UTC 11 Apr 2017	1100 UTC 12 Apr 2017	26	536	11.8	86.1	769	10.1	9.398
0500 UTC 16 Apr 2017	0500 UTC 17 Apr 2017	24	649	13.2	90.1	807	7.9	0.000
0700 UTC 19 Apr 2017	1900 UTC 19 Apr 2017	12	188	7.5	98.1	366	18.3	2.032
1800 UTC 21 Apr 2017	1400 UTC 22 Apr 2017	20	645	14.5	88.5	858	6.7	0.000
1200 UTC 24 Apr 2017	1900 UTC 24 Apr 2017	7	257	8.4	91.7	456	20.1	8.128
Total		3546						664.210
Mean (all)		38.5	363.3	12.0	89.6	570.4	25.9	7.220
Std dev		40.4	151.4	2.8	5.1	150.6	9.6	11.313
Min		6.0	150.0	5.2	74.8	334.9	1.8	0.000
Max		226.0	953.1	19.7	101.0	1086.7	50.0	78.232

The statistical characteristics of each gap-flow case observed at TDE were determined by averaging the consecutive hourly vertical-profile metrics produced by the Neiman et al. (2018) algorithm for that case (Table 2). The statistics for the full 92-case inventory at TDE were established by averaging the mean characteristics of those 92 cases (bottom of Table 2). The cases range in duration between 6 and 226 h, with a mean of 38.5 h, and they account for 34.7% of the total number of hours during this two cool-season period. The mean altitude of the gap-flow jet (i.e., the altitude where the easterly flow is maximized) resides at 363 m MSL, with bounds of 150 and 953 m MSL. These values reside mostly beneath the top of the inner gorge walls at ~700 m MSL (Fig. 1c). The gap-jet mean velocity is 12 m s^{-1} from 89.6°, with case averages as weak and strong as 5.2 and 19.7 m s^{-1}. Atop the gap jet, strong vertical wind shear marks the upper bound of the channeled flow, which was quantified for each case by averaging the hourly zonal shear across the two adjacent wind profiler range gates surrounding the altitude of the hourly gap-flow depth over the duration of the event. The mean magnitude of the capping shear layer is 25.9 m s^{-1} km^{-1} at the mean gap-flow-depth altitude of 570 m MSL, which also resides below the top of the inner gorge. The spread in mean gap-flow depth is considerable, ranging from 335 to 1087 m MSL, with the deepest case occurring at an altitude above (below) the gorge's inner- (outer-) wall rim. Seventy percent of gap-flow cases are associated with accumulating precipitation at TDE. The total precipitation during gap-flow events is 664 mm, or 30% of the total observed during the two winters. Given that gap-flow events constitute 34.7% of this period, these events, collectively, are only slightly drier than average.

To evaluate the mean vertical structure of flows through and above the CRG during the 92 gap-flow events observed at TDE, all 3546 hourly wind profiles were averaged into composite profiles of wind speed and direction and their zonal and meridional components (U and V, respectively) up to ~2.2 km MSL. Collocated surface data were also averaged and then included in the composite profiles. Composite wind profiles were also constructed at WCO (i.e., the gap-flow source region in the Columbia basin) and AST (i.e., the mouth of the Columbia River on the Pacific coast), and composite surface values were generated at six sites from the Columbia basin to the coast, using the same hours as at TDE. For the composite profiles at WCO, which is nearly 400 m above the Columbia River, composite surface data from DLS also were

included to depict flow along the nearby river corridor. All composite profiles described above, together with standard deviation bars, are shown in Figs. 3 and 4 (black lines), and the surface composite counterparts are presented in the first column of Figs. 5 and 6. Although these composites are duplicated to enable subsequent comparison with both gap-flow stratifications (i.e., strength and depth), we initially refer to Figs. 3 and 5 only in our discussion of the 92-case composites.

At the mouth of the CRG at TDE (Fig. 3, middle column), a bimodal 12 m s^{-1} maximum in wind speed and U between 0.2 and 0.5 km MSL define the easterly gap-flow jet. Above the jet, the flow veers to southeasterly at 1 km MSL and to south-southwesterly in the free troposphere above. In the Columbia basin at WCO (Fig. 3, right column), the flow is weaker than at TDE throughout the column, although the easterly flow is deeper—extending up to 1 km MSL before veering to ambient south-southwesterly aloft. The deeper easterlies quite likely reflect deeper cold air in the basin than in the gorge. Along the coast at AST (Fig. 3, left column), there is only weak evidence of remnant gap flow, which confirms the Sharp (2002) model simulation of the spreading and collapsing of gap flow in its exit region where shallow terrain no longer constrains the flow. Shallow southeasterly flow at and near the surface veers to southerly at 1 km MSL and then to ambient southsouthwesterly aloft.

The surface composites in Fig. 5 (left column) show easterly flow at the three sites in the basin and gorge (i.e., HRI, DLS, TDE), veering sharply downriver at SPB to south-southwesterly, and backing farther downriver at KLS to southeasterly and to east-southeasterly at the coast at AST. The directionality of the surface flow from the interior to the coast mirrors the orientation of the Columbia River, hence pointing to channeling of the surface flow by the river corridor during gap-flow conditions. The magnitude of the surface flow is weak (i.e., <3 m s^{-1}) at all sites except TDE, where stronger easterly flow of 7 m s^{-1} is exiting the gorge. Companion SLP composites reveal a ~6.5-hPa downgradient configuration from the interior to the coast. Nearly 70% of that gradient is confined to the adjacent sites flanking the gorge at DLS and TDE. Conditions are coolest and driest in the basin (2°C, 3.8 g kg^{-1}) and warmest and most moist at the coast (8°C, 5.2 g kg^{-1}). A well-defined trend in total precipitation accumulation spans the surface sites, from ~85 mm in the dry continental interior to ~1450 mm at the coast where landfalling storms have maximum impact.
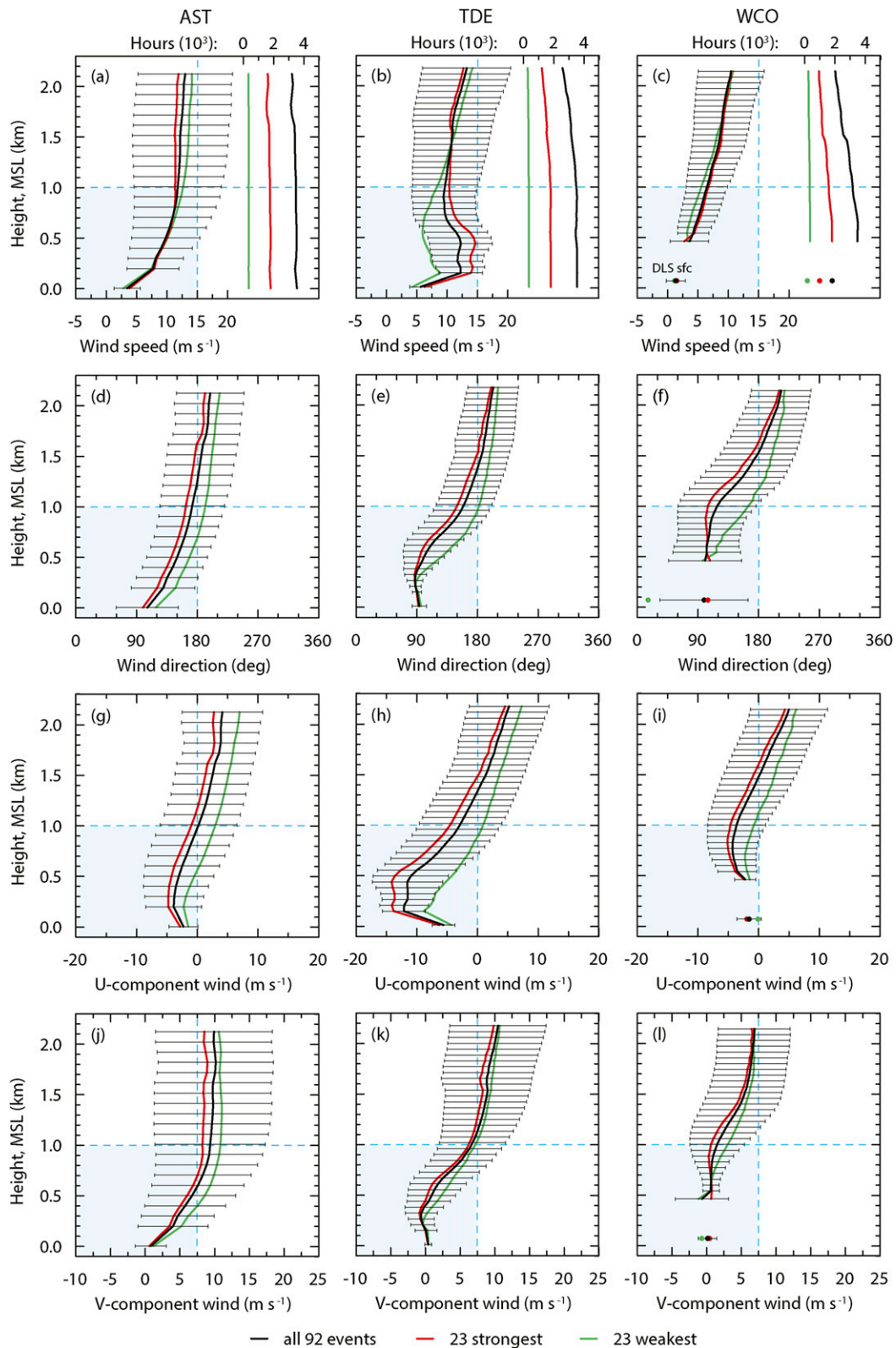
FIG. 3. Composite mean wind profiles with horizontal standard deviation bars (black) at (left) AST, (center) TDE, and (right) WCO, based on the 92 gap-flow cases observed at TDE: (a)–(c) total wind speed

2) STRATIFIED WIND PROFILER COMPOSITES

We stratified the 92 gap-flow cases at TDE into top and bottom quartiles based on the strength of the easterly component in the core of the gap jet and on the depth of the gap flow. Composite wind profiles and surface values were generated for the 23 strongest and weakest cases (19.7–13.7 and 10.2–5.2 m s^{-1}, respectively) and the 23 deepest and shallowest events (1087–667 and 445–335 m MSL, respectively). These stratification classes are composed of 1808, 359, 1365, and 444 h, respectively, and are shown with their composite mean counterparts in Figs. 3 and 4 (red and green profiles) and Figs. 5 and 6 (red and green bars). Table 3 contrasts the stratified statistical results of the mean gap-flow characteristics at TDE.

Stratification results based on gap-jet strength at TDE are presented in Figs. 3 and 5. The vertical structure of the strong composite profiles at TDE (Fig. 3, middle column) mirror those of the full 92-case composite. The magnitude of the total speed and U in the strong composite is slightly larger than in the full composite below 1.5 km, with the greatest difference of $\sim$3 m s^{-1} occurring in the gap-flow layer between 200 and 600 m MSL. In contrast, the weak composite profiles exhibit significant structural differences below 1 km MSL, most notably a shallow and weak gap jet. Above the weak composite gap jet, the flow is rotated 10°–30° clockwise relative to the two other composites. The stratified composite profiles at WCO and AST (Fig. 3, right and left columns, respectively) show comparable contrasts to those at TDE. Table 3 reveals that the strong-quartile events are, on average, much longer lived, deeper, and capped by stronger vertical shear than their weak counterparts. At the surface (Fig. 5), the most notable differences in the strong composites (middle column) relative to their weak counterparts (right column) are: 1) $\sim$4 m s^{-1} stronger surface flow at TDE, 2) $\sim$4 hPa larger pressure difference from the interior to the coast, and 3) uniformly cooler and drier from the interior to the coast.

Composite gap-flow results stratified by depth are presented in Figs. 4 and 6. The vertical structure of the deep-quartile composite profiles at TDE is generally similar to those of the 92-case composites, although the easterly gap jet is 2 m s^{-1} stronger and the flow is rotated counterclockwise by $\sim$10°–30° above the jet, resulting in easterly component flow 400 m deeper (Fig. 4, middle column). In contrast, the shallow gap-flow composite profiles are markedly different than their deep counterparts. Most notably, the gap jet is weaker and closer to the ground and the easterly flow is considerably shallower. Comparable structural differences between the deep and shallow profiles are also observed at WCO and AST (Fig. 4, right and left columns, respectively). The deep events are, on average, longer lived, stronger, and with weaker capping vertical shear than their shallow counterparts (Table 3). At the surface (Fig. 6), the deep events are drier and have a modestly larger along-gorge SLP gradient than their shallower counterparts. Also, the deep events receive roughly half the precipitation as their shallower counterparts despite the fact that the deep events contain three times more hours. We will address this interesting result from a dynamical perspective in the follow-on subsection.

3) STRATIFIED SYNOPTIC-SCALE COMPOSITES

To explore the synoptic-scale control of gap-flow strength and depth at TDE, composite mean analyses are generated from the CFSv2 that correspond to the top and bottom quartiles of these gap-flow metrics (Figs. 7, 8). Those 6-h CFSv2 analyses that fall within the gap-flow date/time ranges shown in Table 2 are included in the gridded composite means. While the CFSv2 is subject to model and data-assimilation changes over time, owing to its operational implementation, these potential changes are not likely to significantly bias or influence the synoptic-scale interpretations of the composite means. A total of 308, 66, 232, and 81 CFSv2 analyses are included in the synoptic composites for the strongest,

---

←

(m s^{-1}), (d)–(f) wind direction (°), (g)–(i) U-component (i.e., zonal) wind speed (m s^{-1}), and (j)–(l) V-component (i.e., meridional) wind speed (m s^{-1}). The wind speeds and directions are scalar averages, whereas the U and V components are vector averages. Also shown in each panel are the mean wind profiles at AST, TDE, and WCO that are stratified by the 23 strongest and weakest gap-flow events observed at TDE (red and green, respectively). The top row also shows profiles of the number of hourly points per range gate for the 92-case mean profiles and the stratified profiles. Composite surface data from DLS accompany the profiles at WCO. The dashed blue lines and shading are shown to help facilitate comparison between panels.
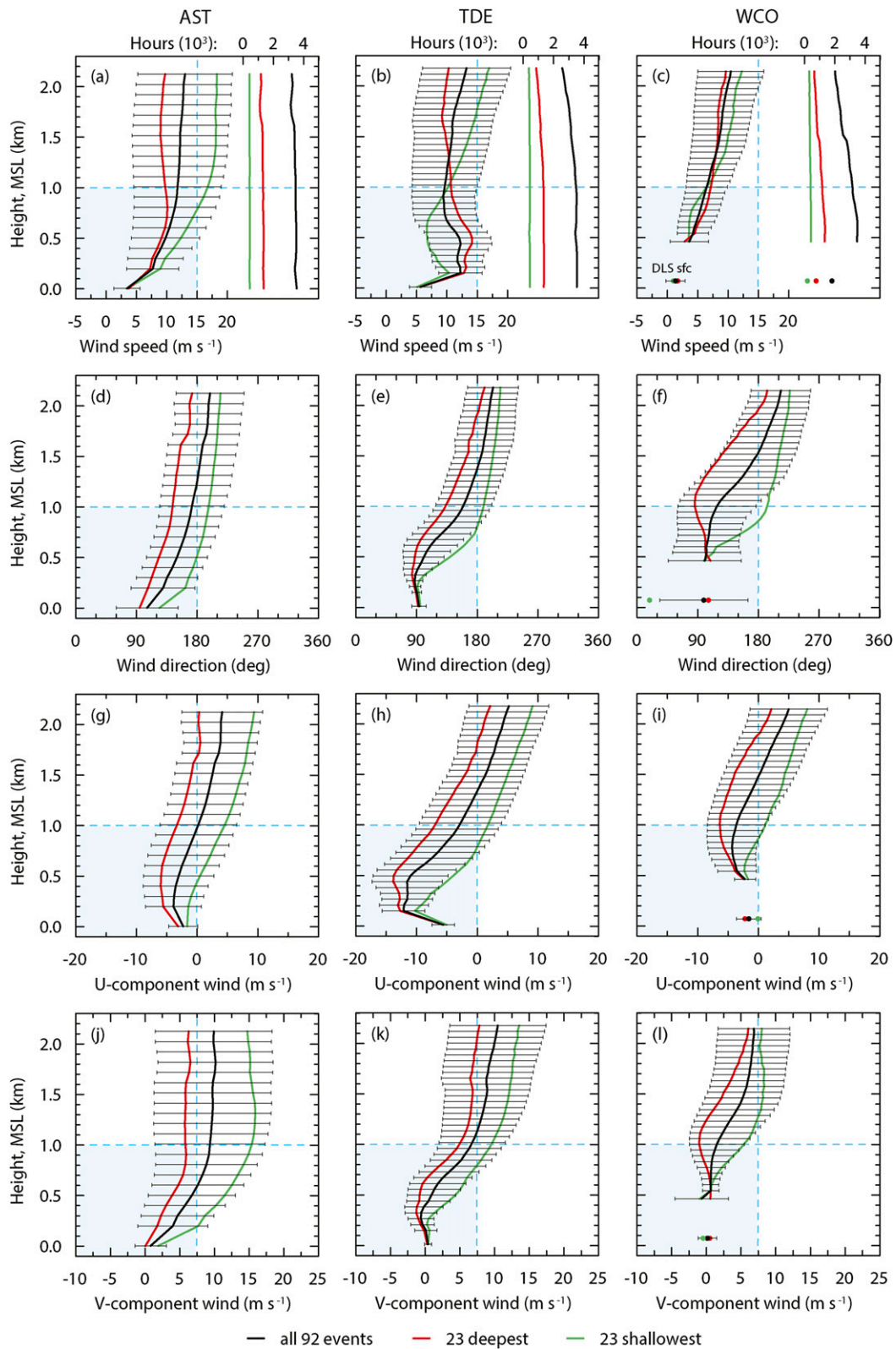
FIG. 4. As in Fig. 3, but for mean wind profiles stratified by the 23 deepest and shallowest gap-flow events at TDE (red and green, respectively).
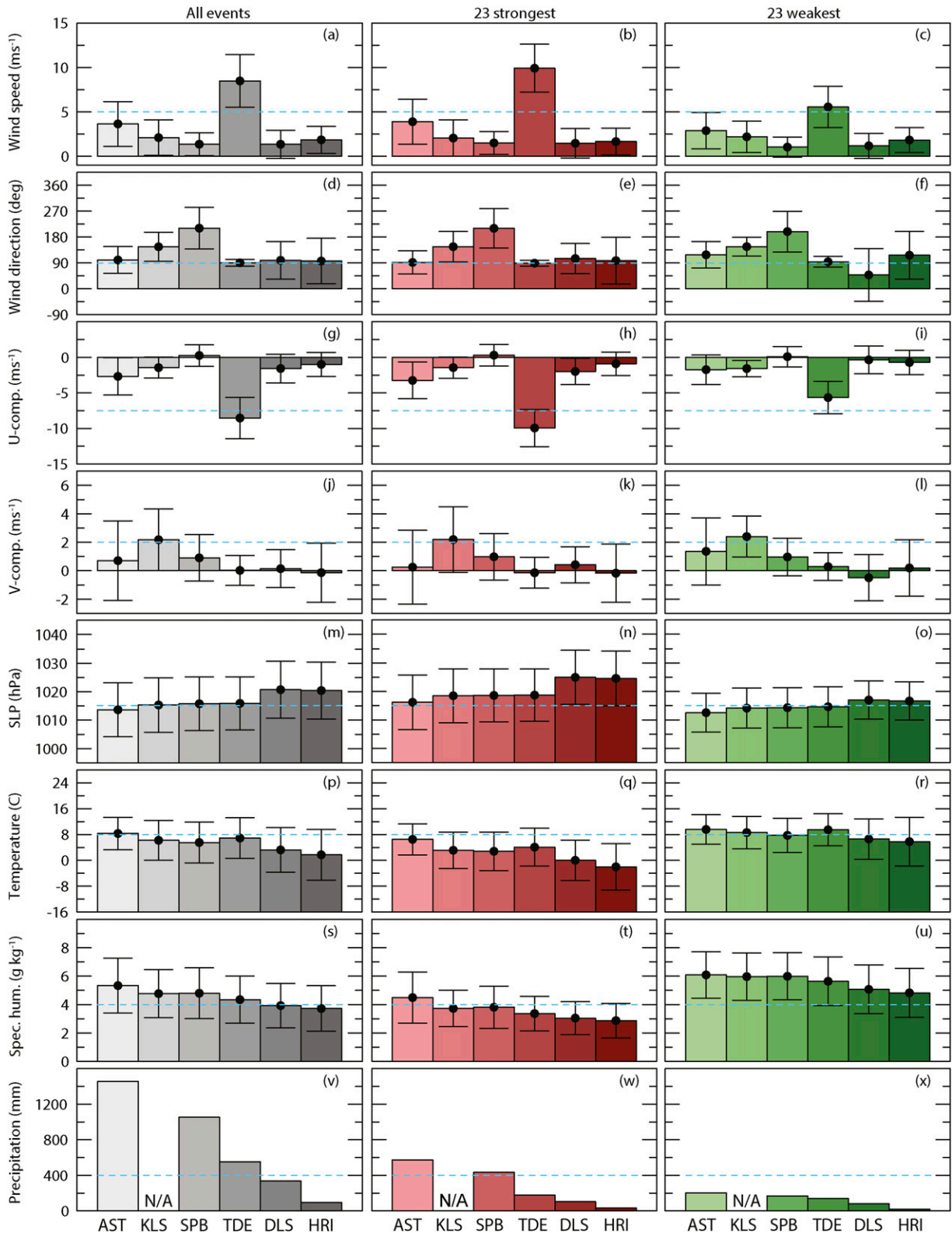
FIG. 5. Composite mean surface data (six sites labeled at the bottom) with vertical standard deviation bars, based on the gap-flow events observed at TDE: (left) all 92 gap-flow events, (center) the 23 strongest gap-flow events, and (right) the 23 weakest gap-flow events. Surface variables include (a)–(c) wind speed (m s^{-1}), (d)–(f) wind direction (°), (g)–(i) U-component (i.e., zonal) wind speed (m s^{-1}), (j)–(l) V-component (i.e., meridional) wind speed (m s^{-1}), (m)–(o) sea level pressure (hPa), (p)–(r) temperature (°C), (s)–(u) specific humidity (g kg^{-1}), and (v)–(x) total precipitation accumulation (mm). Reliable precipitation measurements were unavailable at KLS. The wind speeds and directions are scalar averages, whereas the U and V components are vector averages. The dashed blue lines are shown to help facilitate comparison between panels.
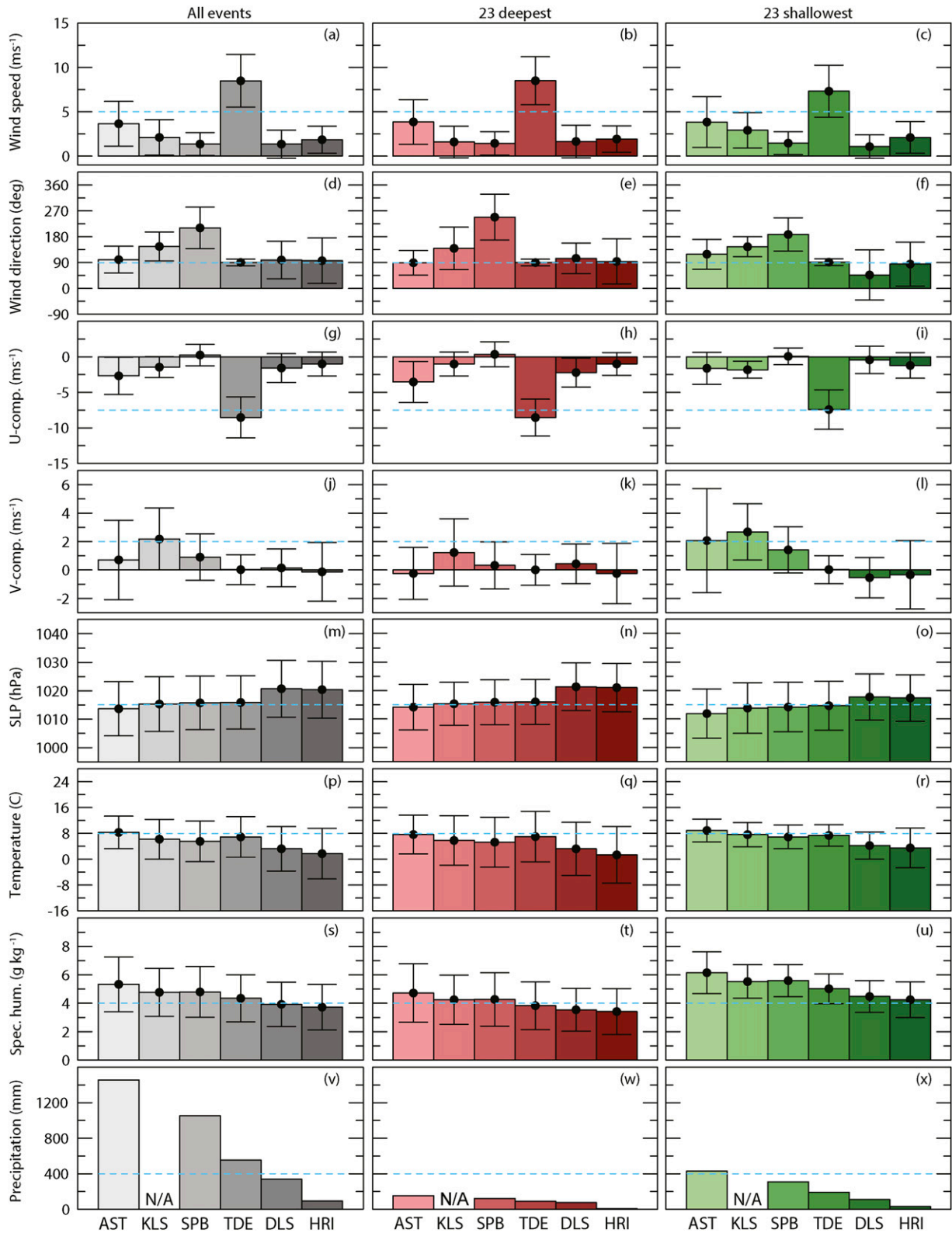
FIG. 6. As in Fig. 5, but for mean surface data stratified by the (center) 23 deepest and (right) 23 shallowest gap-flow events at TDE.

TABLE 3. Composite summary statistics of gap-flow cases from the Troutdale wind profiler for the two cool seasons. In addition to showing the (top row) full 92-case mean values, the results are also stratified by the following characteristics into (middle three rows) upper and lower quartiles of 23 cases each for gap-flow jet strength and (bottom three rows) depth. The wind direction of the gap-flow jet is excluded from this table because there is very little variability about the ~90° mean.

Metric	Gap-flow event (No. of hours)	Gap flow jet: Altitude of max easterly flow (m, MSL)	Gap flow jet: Magnitude of max easterly flow (m s^{-1})	Gap flow depth (m, MSL)	Zonal vertical wind shear atop the gap flow (m s^{-1} km^{-1})
92-case mean	38.5	363.3	12.0	570.4	25.9
Strongest 23, mean	78.6	475.0	15.7	693.4	31.9
Weakest 23, mean	15.6	261.1	8.7	457.9	22.6
2-sided *t*-test significance, strength	100%	100%	100%	100%	99.9%
Deepest 23, mean	59.3	566.2	14.1	779.0	20.9
Shallowest 23, mean	19.3	199.8	10.0	403.0	25.8
2-sided *t*-test significance, depth	99.9%	100%	100%	100%	92.0%

weakest, deepest, and shallowest stratifications, respectively.[1] Composite means are accompanied by their anomaly counterparts, which are calculated by subtracting the long-term (1981–2010) CFSR averages composed of the specified 6-h days/times from the CFSv2 composite mean fields based on those same days/times. These temporally nonoverlapping gridded datasets are both employed because the CFSR (CFSv2) does not extend sufficiently forward (backward) in time.

All four sets of synoptic composites (Figs. 7, 8) display common attributes, including a progressive 1000–500 hPa trough offshore of the CRG, a ridge axis east of the gorge, an axis of warm maritime air at 1000 hPa just offshore of the coast, polar cold-frontal baroclinicity farther offshore, and cold continental air east of the gorge in the Columbia basin. The westward increase in 1000-hPa temperature along the gorge and the associated westward decrease in 1000-hPa geopotential height favor westward-directed gap flows down the pressure gradient in the gorge.

Despite commonalities, these synoptic composites also possess unique attributes, which, ultimately, help explain differences in the wind profiler and surface composite structures described earlier. Focusing first on gap-flow strength, the strong composite at 500 hPa exhibits weaker onshore geostrophic flow than its weak counterpart (Figs. 7a,b), consistent with the upper portion of the wind profile composites at TDE and AST showing stronger flow aloft with weak gap-flow events (Figs. 3a,b). The height anomalies at 500 hPa for the strong gap-flow composite show a weaker offshore minimum and a stronger interior maximum than the

weak gap-flow composite. This anomaly dipole is oriented southwest-northeast for the strong composite and northwest–southeast for the weak composite. Similar anomaly characteristics are found in the 1000-hPa height composites (Figs. 7c,d), resulting in a stronger westward decrease in geopotential height along the gorge for the strong gap-flow events. The companion temperature composite at 1000 hPa for strong cases reveals (Fig. 7e) widespread cold air over the northern Rockies and Columbia basin. The prevalence of ridging aloft in the northern interior favors the development of cold arctic anticyclogenesis in the lower troposphere in combination with boundary layer radiative cooling. In contrast, much weaker ridging aloft in the northern interior for the weak gap-flow cases is unfavorable for arctic anticyclogenesis or boundary layer cooling, hence cold air is absent in the interior at 1000 hPa (Fig. 7f). Correspondingly, the weak gap-flow composite at the WCO wind profiler (Fig. 3f) reveals shallow easterly flow, most likely due to the lack of a significant cold pool. In summary, the strong gap-flow events are governed by a cold interior anticyclone whereas the weak events are dominated by an offshore cyclone.

The synoptic composites for deep-versus-shallow gap-flow events (Fig. 8) resemble those of the strong-versus-weak events (Fig. 7), consistent with the fact that strong (weak) events are typically deep (shallow) (Table 3). Nevertheless, there are substantial differences in the details. The deep gap-flow composites (Figs. 8a,c) show negative height anomalies offshore that are larger and displaced southeast of the corresponding strong gap-flow anomalies (Figs. 7a,c). Simultaneously, the interior positive height anomalies in the deep composites are northwest of and larger than the strong composites. These changes yield low-level geostrophic flow with a more pronounced westward component near and offshore of the coast for the deep gap-flow events (Fig. 8c),

---

[1] Randomized composite experiments were conducted to explore possible biases resulting from differing sample sizes. No significant differences were found.
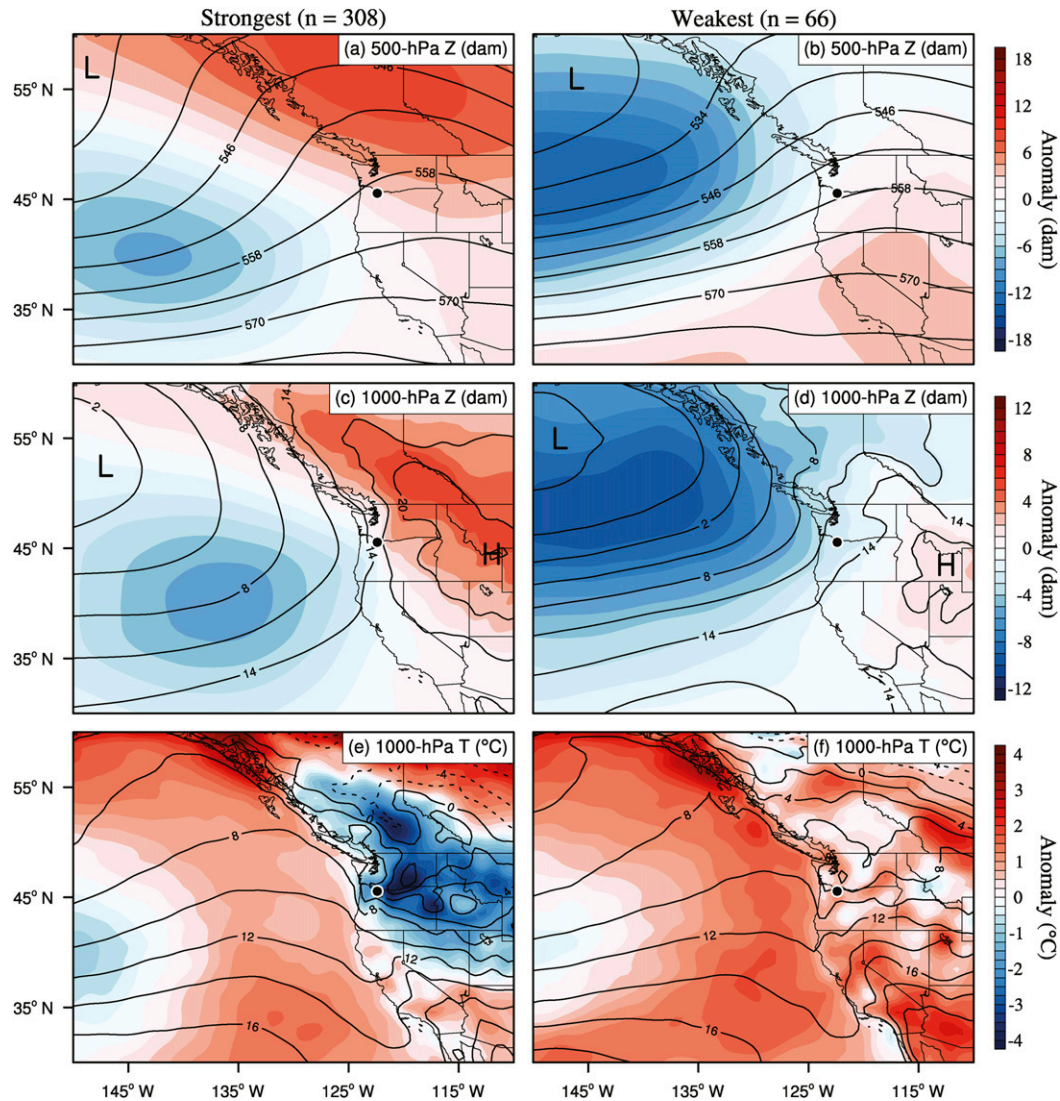
FIG. 7. Composite mean and anomaly analyses (solid and color-filled contours, respectively) derived from NOAA's Climate Forecast System gridded datasets, stratified by the (left) 23 strongest and (right) 23 weakest gap-flow events observed at TDE (location shown by black dot): (a),(b) 500-hPa geopotential height (dam); (c),(d) 1000-hPa geopotential height (dam); and (e),(f) 1000-hPa temperature (°C). The anomaly reference period is 1981–2010. The variable *n* at the top of each column shows the number of 6-h analyses used in the strong and weak composites.

which suggest that such events represent a combination of channeled and synoptically forced flow. Correspondingly, the deep gap-flow composite wind profiles (Figs. 4d–f) show wind direction profiles through their 2.3-km depth that are rotated counterclockwise relative to the 92-case and shallow composites. Finally, the deep cases have warmer interior temperatures and colder offshore temperatures than the strong ones (Figs. 8e, 7e), which further suggests that these deeper cases are not driven solely by the magnitude of the interior cold pool or low-level temperature (and, by extension, SLP)

gradient along the gorge but also require phasing with synoptic-scale forcings.

b. Temporal evolution

We now explore the composite temporal evolution of the 92 gap-flow events observed at TDE. Hourly data from these events have been placed into 20 equally distributed temporal bins and then averaged, where time is expressed as a normalized fraction of the total gap-flow duration (Figs. 9, 10). Composite temporal characteristics of gap-jet strength and gap-flow depth are
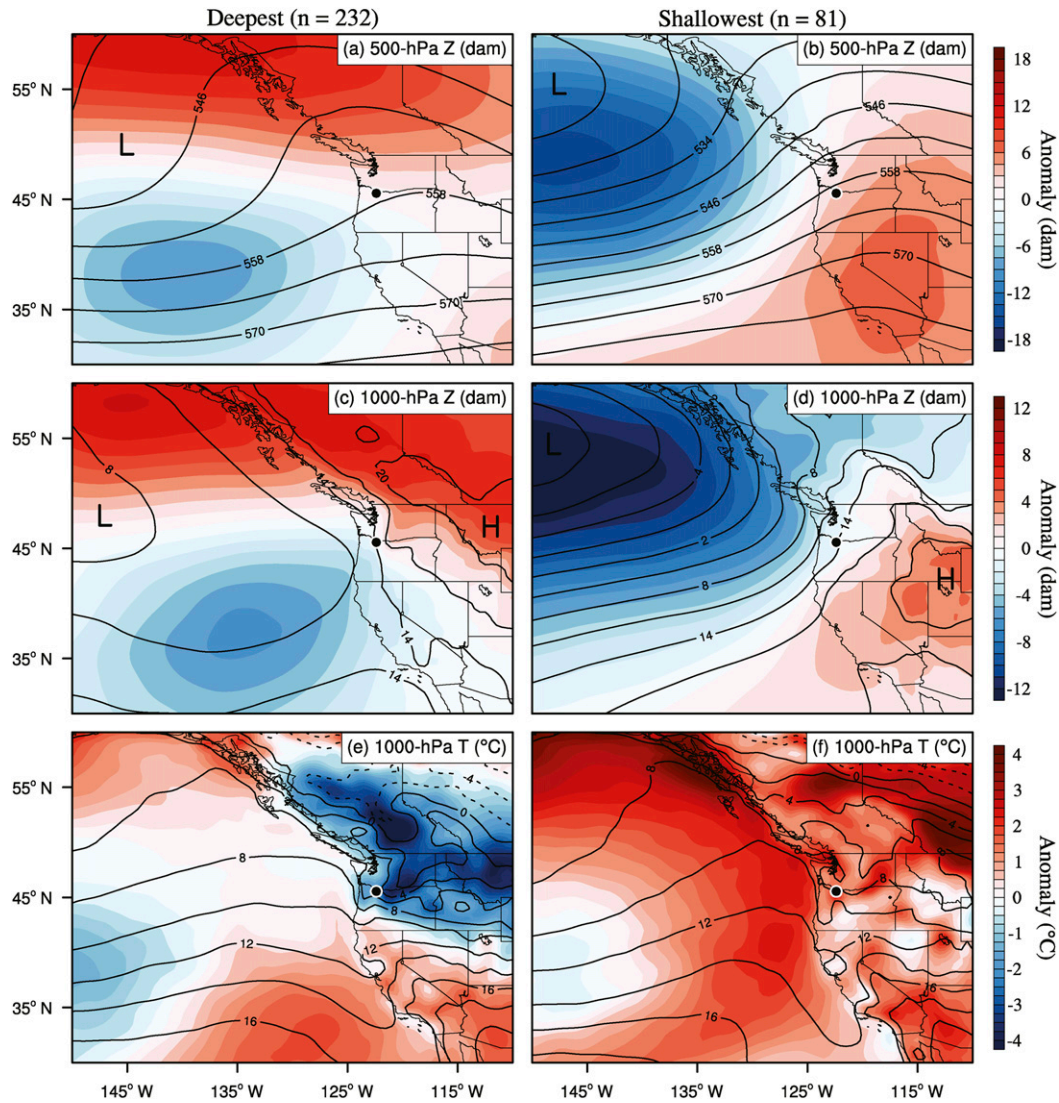
FIG. 8. As in Fig. 7, but stratified by the (left) 23 deepest and (right) 23 shallowest gap-flow events observed at TDE.

presented in Figs. 9a and 9b, respectively, where these metrics are determined on an hourly basis using the gap-flow auto-detection algorithm in Neiman et al. (2018). The average magnitude of the gap jet commences weak, strengthens to $>\sim15\,\mathrm{m\,s^{-1}}$ during the middle of the composite event, and subsequently weakens. The greatest number of hourly gap-jet speeds in the bottom quartile ($\leq10.8\,\mathrm{m\,s^{-1}}$) populate the wings of the event, while those hourly speeds in the top quartile ($\geq16.8\,\mathrm{m\,s^{-1}}$) concentrate in the middle of the event. Above the gap flow at 1.5 km MSL, weak southeasterly flow of $\sim5\,\mathrm{m\,s^{-1}}$ strengthens to $7.5\,\mathrm{m\,s^{-1}}$ southerlies during peak gap-jet strength, and the flow continues to strengthen and veer to $\sim12.5\,\mathrm{m\,s^{-1}}$ southwesterlies with the approach of an offshore trough and associated polar cold front. The mean depth of the composite gap-flow event commences

at 600 m MSL, increases to 700 m MSL 17.5% into the event, and then decreases thereafter (slowly at first, then more quickly). The greatest number of top-quartile hourly depths ($\geq770\,\mathrm{m}$ MSL) occur during the middle of the event, while the bottom-quartile depths ($\leq470\,\mathrm{m}$ MSL) are skewed to the final 20% of the event. The simultaneous decrease in gap-flow depth with the increase in maritime southwesterlies aloft suggest that the gap flow is eroding via vertical turbulent mixing.

The composite temporal evolution of hourly SLP tendency at TDE and DLS at opposite ends of the gorge and of the along-gorge pressure gradient between DLS and TDE are shown in Fig. 9c. The tendency at TDE ranges between -0.15 and $-0.4\,\mathrm{hPa\,h^{-1}}$ for most of the composite due to an approaching landfalling cyclone, whereas the final temporal bin changes sign with
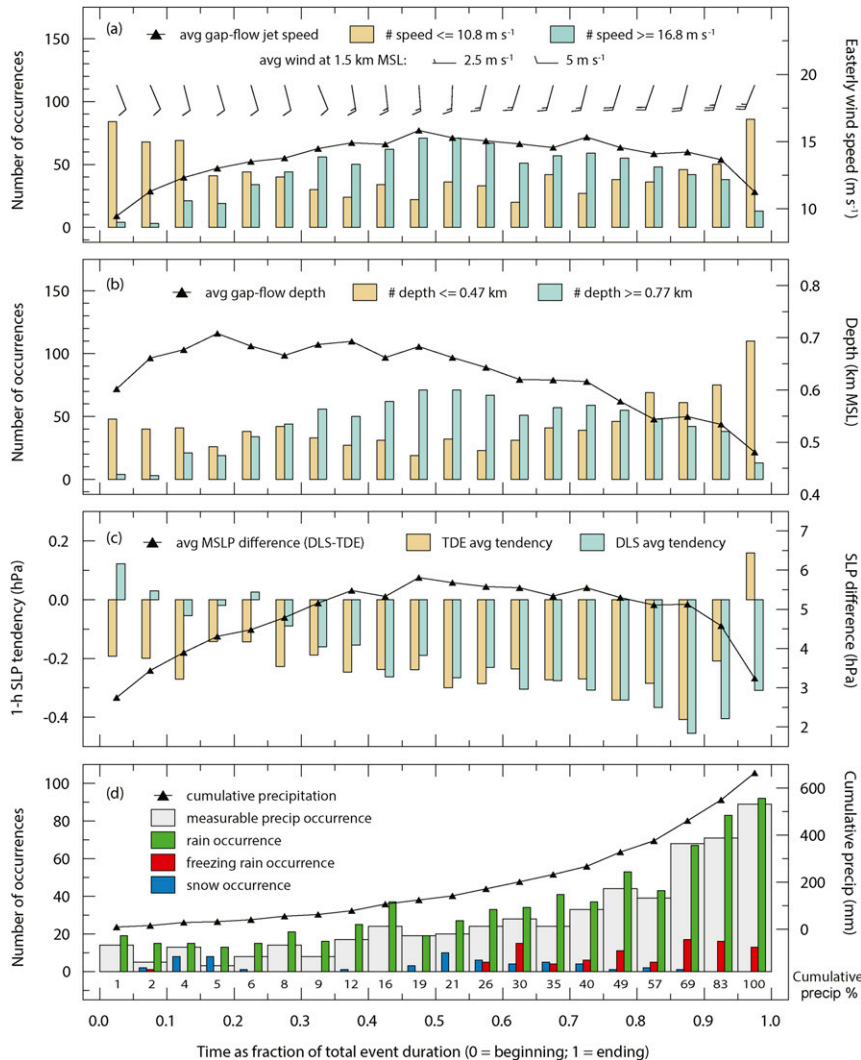
FIG. 9. Composite normalized temporal distribution of key observations during the 92 gap-flow events observed at TDE, where time is expressed as the fraction of the total event duration (beginning = 0, end = 1, interval = 0.05). (a)–(c) All 3546 1-h periods during the gap-flow events, and (d) the 565 1-h periods with measureable precipitation during those events. (a) Wind velocity at TDE. Histogram bars (see key): number of 1-h occurrences in the bottom and top quartiles of easterly wind speed ($\leq$10.8 and $\geq$16.8 m s^{-1}, respectively) in the core of the gap jet. Black curve: average easterly wind speed (m s^{-1}) of the gap jet. Wind barbs (barbs: 5 m s^{-1}; half-barbs: 2.5 m s^{-1}): average wind velocity at 1.5 km MSL. (b) Gap-flow depth at TDE. Histogram bars (see key): number of 1-h occurrences in the bottom and top quartiles of gap-flow depth ($\leq$0.47 and $\geq$0.77 km MSL, respectively). Black curve: average depth of the gap flow (km MSL). (c) SLP characteristics at TDE and DLS. Histogram bars (see key): Average 1-h SLP tendency (hPa) at TDE and DLS. Black curve: SLP difference (hPa) between DLS and TDE. (d) Precipitation characteristics at TDE. Histogram bars (see key): number of 1-h occurrences with measureable precipitation, rain, freezing rain, and snow. Black curve: cumulative precipitation starting at time = 0. The cumulative precipitation percentage (rounded to the nearest whole number) is shown below each histogram-bar grouping.

the initial passage of a polar cold front. The tendency at DLS is initially >0, quite likely in response to building high pressure in the continental cold pool in the Columbia basin. After one-quarter of the composite event transpires, the tendency becomes consistently negative with the approach of the Pacific cyclone. During the final 30% of the composite, the negative SLP tendency is larger at DLS than at TDE, quite likely
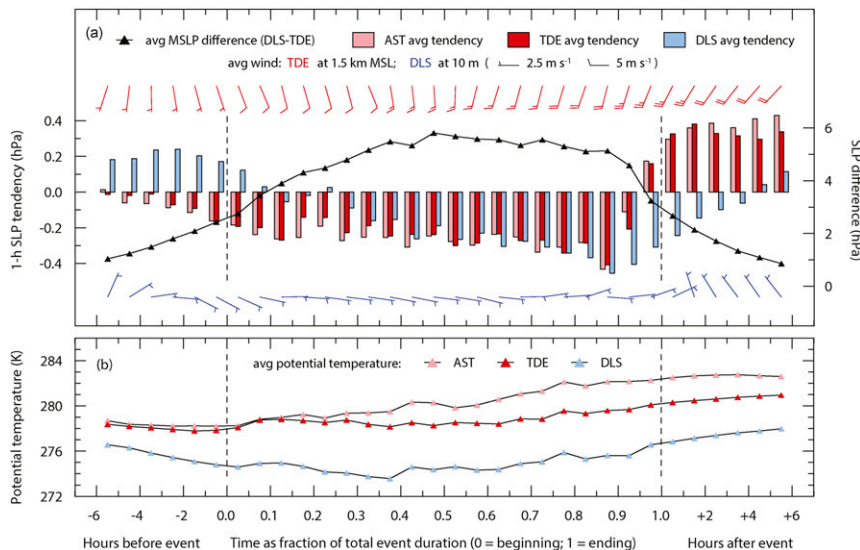
FIG. 10. (a) As in Fig. 9c, but that the time axis extends ±6 h beyond the outer bounds of the composite gap-flow event (vertical dashed lines), the color key is different, the SLP characteristics at AST are included, and the average 1-h near-surface wind barbs at DLS and 1.5 km MSL barbs at TDE are also included. (b) Corresponding time series of composite potential temperature (K) at AST, TDE, and DLS (see key).

because the depth of the interior cold pool is decreasing with vertical turbulent mixing from strengthening southwesterlies aloft. The SLP gradient between DLS and TDE increases from 2.75 hPa at the start of the composite to nearly 6 hPa at the half-way mark and then decreases to 5.13 hPa at 90% through the event. In the last 10%, the SLP gradient decreases markedly with the initial polar cold-frontal passage at TDE. Comparing the composite time series of SLP gradient with gap-jet speed reveals a high correlation of 0.98, consistent with Sharp and Mass (2004) who show $r^2 = 0.80$ for hourly surface easterly wind speed at TDE versus hourly SLP gradient between DLS and TDE during a 2-yr period. Similarly, the wind profiler study of Neiman et al. (2006) highlights a 5.75-day gap-flow case through California's Petaluma Gap, where $r^2 = 0.86$ for the hourly relationship between easterly component flow in the 250–550 m MSL layer versus the along-gap SLP gradient. A physical link is absent between the DLS–TDE SLP gradient and gap-flow depth at TDE, where $r^2 = 0.05$.

To gain additional meteorological insights on gap-flow evolution, a temporally expanded version of Fig. 9c is shown in Fig. 10, which also includes the following new hourly averaged data: SLP tendency at the coast at AST, surface wind at DLS, and 2-m potential temperature (θ) from all three sites. SLP tendencies west of the gorge at TDE and AST track in unison throughout the composite time series, including during the SLP rises following gap-flow conditions with the composite polar cold-frontal

passage (Fig. 10a). The θ at TDE and AST also track in unison, but only prior to, and at the onset of, gap-flow conditions (Fig. 10b). Thereafter, steady warming ensues at AST in the precold-frontal maritime air mass, whereas warming doesn't commence at TDE until ~60% through the composite gap-flow event. The wind shift with the cold-frontal passage at 1.5 km MSL is captured late in the time series, where strong precold-frontal southwesterlies veer and weaken in conjunction with the SLP rises at TDE and AST (Fig. 10a). During this period, θ along the coast at AST starts to decrease slightly in postcold-frontal conditions, while it continues to increase at TDE as the gap flow erodes at the mouth of the gorge (Fig. 10b). The SLP tendency at DLS exhibits markedly different characteristics than at its western counterparts. Namely, rises are observed during the lead-in to gap-flow conditions as the Columbia basin shallow cold pool intensifies (note the companion decrease in θ), while, during the cessation of gap-flow conditions, falls transition to weak rises as the influence of the interior cold pool wanes and postfrontal ridging increases. During this latter period, the surface flow at DLS transitions from easterly to northwesterly and the surface θ attains its warmest values, likely in response to increasing postcold-frontal downslope westerly component flow aloft east of the Cascades eroding the cold pool from above (e.g., Whiteman et al. 2001).

Figure 9d highlights temporal characteristics of hourly precipitation at TDE during the composite gap-flow

event when 664 mm accumulates. It starts relatively dry, where 19% of the accumulation occurs during the first half of the composite, and ends wet, where nearly one-third accumulates in the last 10%. Measureable precipitation and rain occurrences are skewed to the latter part of the event. The increasing wetness with time coincides with the landward approach of extratropical cyclone conditions and polar cold fronts. The temporal distribution of snow and freezing rain differ from each other and from rain. Namely, snowfall is favored during the early stage of gap-flow events when cold gap flow is deepest and during the middle of the events when the gap jet is strongest. In contrast, freezing rain occurs during the latter half of gap-flow events when the depth of the cold gap flow is decreasing significantly with the advection of warm and moist southwesterly precold-frontal flow ahead of a progressive trough aloft.

Another aspect of temporal evolution to consider is whether there are any diurnal or interseasonal impacts on gap flows. Figure 11 presents diurnal histograms of event begin times and end times and monthly (cool-season) histograms of hourly gap-flow occurrence for the full 92-case inventory. The event begin times (Fig. 11a) are grouped mainly in the evening local time (LT). For example, 54 (i.e., 59%) of event begin times are between 0100 and 0900 UTC (i.e., 1700–0100 LT), with a maximum number (14) occurring at 0500–0600 UTC (2100–2200 LT). This makes sense because cold pooling contributes to gap flow development, and cold pooling is maintained by radiational cooling during the night. In contrast, the end times occur more often during the morning hours LT (Fig. 11b). Consequently, 45 (i.e., 49%) of the event end times are between 1200 and 2000 UTC (0400–1200 LT), with a maximum number (10) occurring at 1900–2000 UTC (1100–1200 LT) and a majority (26) within this period occurring between 1700 and 2000 UTC (0900–1200 LT). This makes sense because turbulent mixing associated with daytime heating can erode the interior cold pool (Zhong et al. 2001) and cause gap flows to diminish. The distributions of gap-flow depth and jet speed did not exhibit any notable diurnal behavior (not shown).

During the cool-season, 1026 h of gap flow (29% of the total observed hours) occurred in January (Fig. 11c), which was nearly twice the number of occurrences in the second and third highest ranked months of December and February (533 and 576 h, respectively). This mid-winter signal coincided with longer-duration events (red text in Fig. 11c), where 811 (79%) of the January gap-flow hours occurred during the longest-quartile events (Table 2) and were associated with an anomalously amplified synoptic-scale trough (ridge) of low (high) pressure over the eastern Pacific Ocean (Pacific
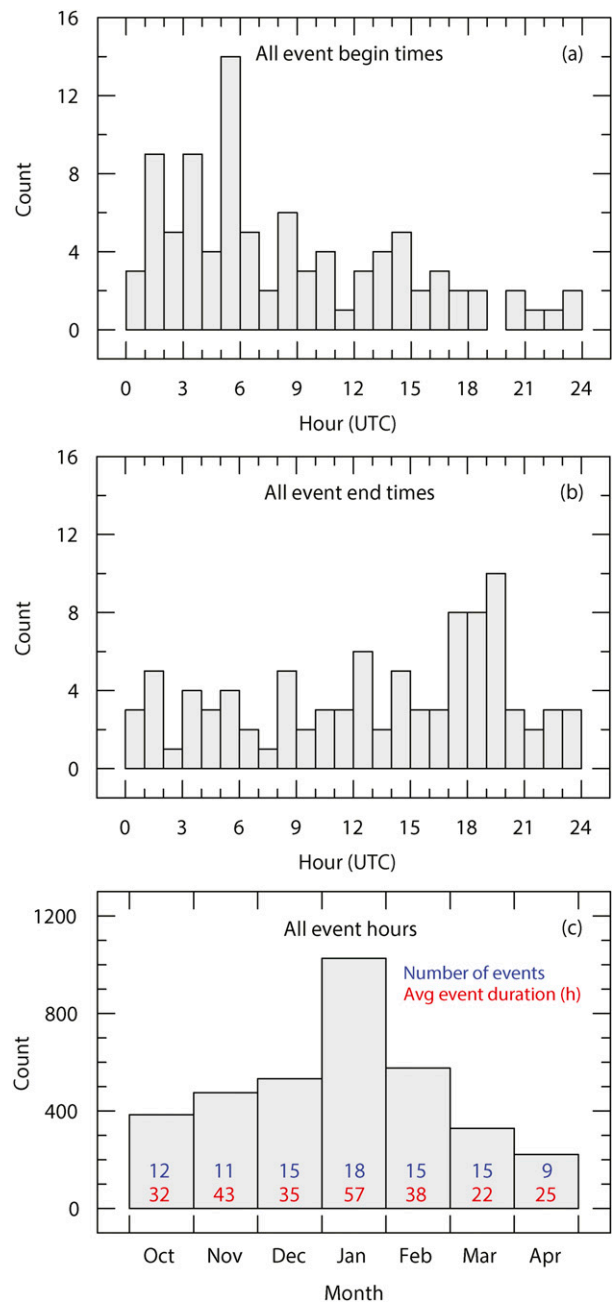

FIG. 11. Hourly distribution of (a) begin time and (b) end time, and (c) monthly distributions of hourly gap flow, for all 92 observed gap-flow events at TDE. The number of events (blue text) and average event duration (h; red text) for each month are shown at the bottom of the histogram bars in (c). Events that spanned month boundaries (November–December 2015; December–January 2015/16; January–February 2017) were split into six events.

Northwest and western British Columbia), which maintained strong radiational cooling and arctic outbreaks east of the CRG and warm advection off the Pacific Northwest coast (not shown).
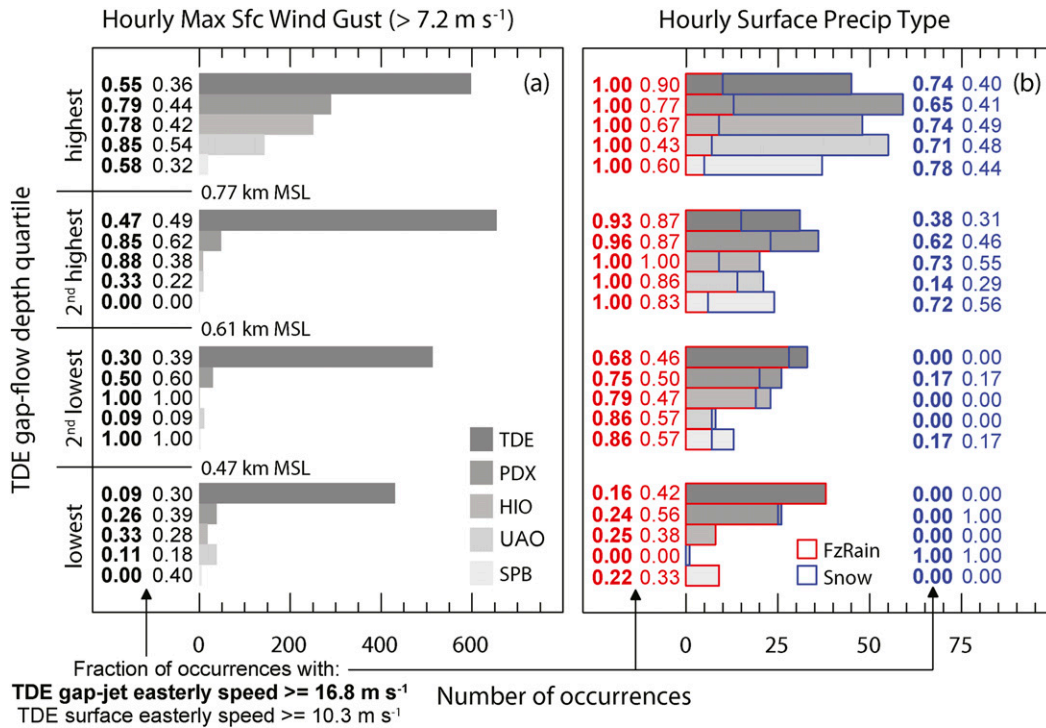
FIG. 12. Composite analysis of regional gap-flow impacts based on the 92-case gap-flow inventory observed at TDE: the number of occurrences of reported hourly (a) maximum surface wind gusts (i.e., $\geq 7.2 \, \mathrm{m \, s^{-1}}$); and (b) winter precipitation type (red = freezing rain, blue = snow), observed at five surface sites in the Portland area (see gray-shaded key in (a) as a function of gap-flow depth (divided into four quartiles: >0.77 km MSL, 0.61–0.77 km MSL, 0.47–0.61 km MSL, and <0.47 km MSL). The fraction of occurrences with gap-jet easterly speeds exceeding $16.8 \, \mathrm{m \, s^{-1}}$ at TDE (i.e., the top quartile of gap-jet values) are expressed numerically for the hourly occurrence of maximum surface wind gusts [left side of (a), bold black font], freezing rain [left side of (b), bold red font], and snow [right side of (b), bold blue font] at each of the five surface sites. The fraction of occurrences with surface easterly speeds exceeding $10.3 \, \mathrm{m \, s^{-1}}$ at TDE (i.e., the top quartile of surface values) are also expressed numerically for the hourly occurrence of maximum surface wind gusts [left side of (a), regular black font], freezing rain [left side of (b), regular red font], and snow [right side of (b), regular blue font] at each of the five surface sites.

4. Gap-flow impacts in the Portland metropolitan area

Gap-flow events can result in strong winds and winter-type precipitation, both of which generate adverse societal impacts in the CRG and westward across the Portland metropolitan area. In this section, we first present a composite analysis (Fig. 12) showing linkages between gap-flow depth and strength observed by the TDE wind profiler during the 92 gap-flow cases and the resulting surface wind and precipitation impacts there and at four other sites around Portland (i.e., at PDX, HIO, UAO, SPB). We then showcase three gap-flow events contained in the inventory to highlight further gap-flow characteristics that generate those impacts (Fig. 13). The gap-flow depth and gap-jet easterly speed are determined hourly using the auto-detection algorithm in Neiman et al. (2018).

The histograms in Fig. 12a depict the number of occurrences of hourly maximum wind gusts exceeding the minimum reported $7.2 \, \mathrm{m \, s^{-1}}$ at the five surface sites as a

function of gap-flow depth (divided into four quartiles). By far, the greatest number of surface gusts occur at the mouth of the CRG at TDE, totaling in the hundreds regardless of gap-flow depth. In contrast, farther west across the Portland metropolitan area at PDX, HIO, and UAO, gusty surface winds are associated primarily with the deepest quartile of gap flows. At the far-downriver site at SPB, gusty surface conditions are rare, regardless of gap-flow depth. The companion histograms in Fig. 12b show the number of occurrences of hourly winter-type precipitation at the five surface sites as a function of gap-flow depth. At TDE and PDX, the number of freezing rain hours mostly increase with decreasing gap-flow depth, consistent with snow melting to rain in the warm air aloft and refreezing on contact with the surface in shallow, cold gap-flow conditions. For the three remaining surface sites located farther downwind of the CRG, the occurrence of freezing rain is not linked substantively to the depth of the gap flow. The number
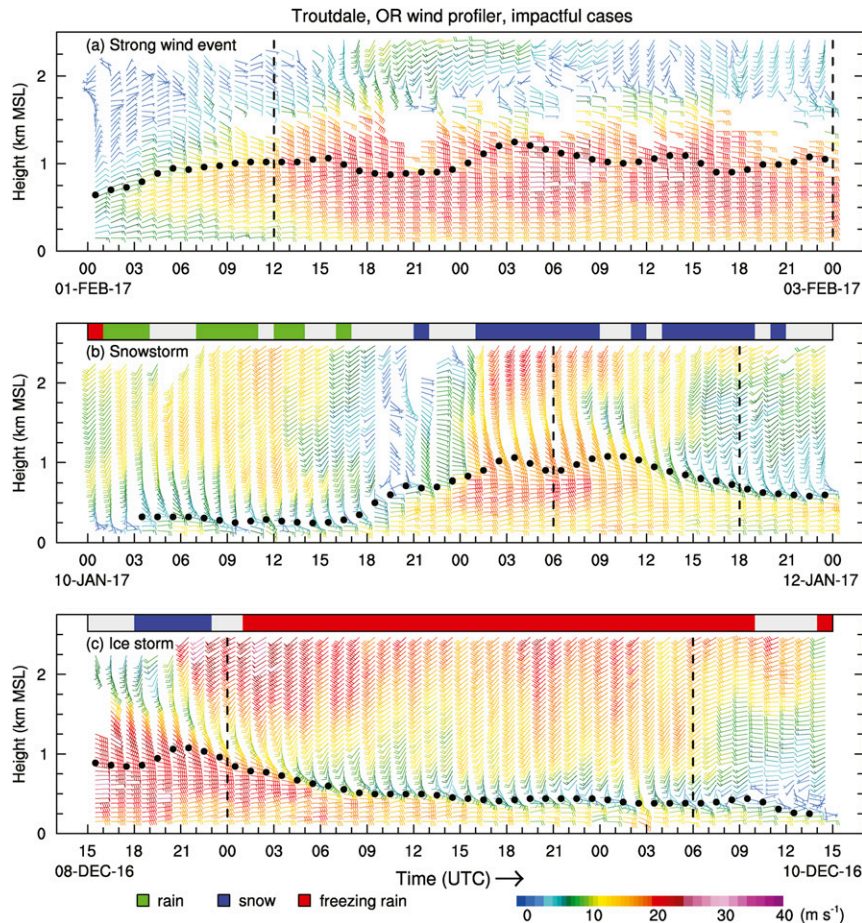
FIG. 13. Time–height sections of impactful gap-flow events measured by the 915-MHz wind profiler at TDE: (a) strong wind event, between 0000 UTC 1 Feb and 0000 UTC 3 Feb 2017; (b) snowstorm, between 0000 UTC 10 Jan and 0000 UTC 12 Jan 2017; and (c) ice storm, between 1500 UTC 8 Dec and 1500 UTC 10 Dec 2016. Wind flags and barbs, color-coding (color bar at bottom), and black dots are as in Fig. 2a. The horizontal color bars in (b) and (c) show the predominant hourly precipitation type (color key at bottom). The pair of vertical black dashed lines in each panel represent the temporal endpoints of the 6-h gridded dataset times used to construct the corresponding case-composite analyses in Fig. 14.

of snow reports is directly proportional to the depth of the gap flow, and the deepest gap-flow conditions yield, by far, the greatest number of such reports. This scenario is consistent with the notion that deep, cold gap flow creates conditions whereby the atmospheric column is less likely to possess above-freezing temperatures to melt snow. Last, the deepest quartile produces regionally homogenous snow occurrences, whereas the shallowest two quartiles yield a decrease in freezing-rain occurrences with increasing distance from the CRG.

The bold column-aligned numerical values in Fig. 12a are the fractional occurrences of hourly maximum surface wind gusts exceeding $7.2 \, \mathrm{m \, s^{-1}}$ at the five surface sites when gap-jet easterly wind speeds at TDE exceed the top-quartile value of $16.8 \, \mathrm{m \, s^{-1}}$. For these strong

gap-jet conditions, roughly half the surface wind gust occurrences at TDE are observed in the two deepest gap-depth quartiles, with much smaller fractional occurrences in shallow gap-flow conditions. At PDX, HIO, and UAO, large fractional occurrences of gusty surface winds for strong gap-jet conditions (i.e., 0.78 to 0.85) far exceed that at TDE in the deepest gap-depth quartile. Hence, strong gap-jet flow at TDE is a more robust indicator of gusty surface winds across the Portland area than at the mouth of the gorge at TDE, especially when the gap flow is deep. We also explore the impact of the top quartile of hourly surface easterly wind speeds at TDE (i.e., $\geq 10.3 \, \mathrm{m \, s^{-1}}$) on the fractional occurrence of gustiness at the five Portland-area sites (regular-font column). For strong surface easterly flow at TDE with

the deepest gap-flow conditions, the fractional occurrences of gusty winds (i.e., 0.32 to 0.54) decrease significantly at all five sites relative to those fractional values based on strong gap-jet conditions. Consequently, using gap-jet easterly wind speed instead of the surface-wind counterpart at TDE provides value-added information on wind impacts across the Portland area.

The bold (regular) numerical values in Fig. 12b represent the fractional occurrences of freezing rain and snow at the five surface sites when gap-jet (surface) easterly wind speeds at TDE exceed the top-quartile value of 16.8 (10.3) m s^{-1}. For the top two gap-flow depth quartiles, nearly all occurrences of freezing rain across the Portland area (0.93–1.00) are associated with strong gap-jet easterly flow, while fewer fractional occurrences of freezing rain (0.43–1.00) are tied to strong easterly flow at the surface. For the second shallowest gap-depth quartile, these fractional occurrences decrease for both of the easterly wind speed metrics, although they are still larger for the gap-jet speeds. The shallowest gap-depth quartile shows no useful linkage between easterly wind speed and the fractional occurrence of freezing rain. Snowfall across Portland is most prevalent in the deepest gap-depth quartile, so we focus on that quartile where strong gap-jet speeds yield significant fractional occurrences of snow (0.65–0.78). These fractional occurrences are smaller (0.40–0.49) for easterly surface wind speeds. As with surface wind gusts across the Portland area, using gap-jet easterly wind speed instead of the surface-wind counterpart at TDE provides value-added information on winter-type precipitation.

Examples of the most impactful cases related to strong wind, snow, and freezing rain are highlighted in bold in Table 2 and are summarized in Table 4 in terms of downstream weather impacts, synoptic characteristics, and gap-jet-strength and gap-flow-depth relationships previously established in this section. The vertical and temporal evolution of each case is depicted by time–height sections of wind profiles and gap-flow depth in Fig. 13, and key synoptic-scale characteristics are represented by case composites of 500-hPa geopotential height and 1000-hPa temperature in Fig. 14. Consistent with the composite-impacts results in Fig. 12, both the strong-wind and snow events possess gap-jet strength and gap-flow depth that are in the top quartile, whereas for freezing rain the gap-jet strength (gap-flow depth) comprise the middle-two (lowest-two) quartiles. In addition, the synoptic-scale controls for these three events are consistent with the results of this study and Sharp and Mass (2004). Specifically, the strong-wind case mirrors the composite stratifications for gap-jet strength and gap-flow depth, while both the snowstorm and ice storm cases are similar in character to the precipitation-type composites in Sharp and Mass.

5. Summary and conclusions

This study utilized unique, temporally continuous, vertical data collected by three wind profilers during two cool seasons between October 2015 and April 2017 to provide a comprehensive observational characterization of the composite vertical and temporal structure of westward-directed gap flows along the Columbia River corridor from the interior basin to the coast, with an emphasis on the exit region of the gorge at TDE. During this period, the TDE wind profiler observed 92 gap-flow cases (44 in year 1 and 48 in year 2) spanning 3546 h.

Vertical-composite analysis provided quantitative depiction of gap flows through the CRG using the methodology described by Neiman et al. (2018) to detect structural characteristics such as gap flow jet speed and depth. The mean gap-jet speed at TDE was 12 m s^{-1}, and the mean altitude of the jet was observed at 363 m MSL. A mean gap-flow depth of 570 m MSL was situated below the top of the inner gorge, while the deepest gap-flow depth was 1087 m MSL–entirely within the gorge's outer-wall rim. The mean gap-flow depth was deepest in the cold-air source region east of the gorge and decreased westward to the coast (1 km at WCO, 0.61 km at TDE, and <0.1 km at AST), which confirms model simulations by Sharp (2002). The gap-flow cases were stratified by strength and depth at TDE. Strong gap-flow events were, on average, longer lived, deeper, and capped by stronger vertical shear than their weak counterparts. Companion CFSv2 reanalysis composites revealed that strong events were governed by a cold interior anticyclone whereas the weak events were dominated by an offshore cyclone. The deep gap-flow events were, on average, longer lived, stronger, and with weaker capping vertical shear than their shallow counterparts. Deep events were associated with geostrophic offshore flow in the lower troposphere, which suggests that such events represented a combination of gap-flow and synoptic forcing.

Temporal-composite analysis provided physical insight into the evolution of CRG gap flows, which comprised five dominant phases. First, prior to gap-flow initiation, a cold pool forms in the Columbia basin through persistent longwave radiative cooling and/or the advection of an arctic air mass. Gap flow ensues in the CRG as the interior cold pool intensifies, and as negative SLP tendencies associated with an approaching offshore synoptic-scale frontal wave are first observed west of the CRG. The second phase represents mature gap flow, where the deepest gap flow is maintained

TABLE 4. Summary information for the three high-impact case studies shown in Fig. 13.

Topic	Event type		
	Strong wind	Snowstorm	Ice storm
Date/time period	1200 UTC 1 Feb to 0000 UTC 3 Feb 2017	0200 UTC 11 Jan to 1900 UTC 11 Jan 2017	2200 UTC 8 Dec to 1100 UTC 10 Dec 2016
Gap-jet strength[a]	20–25 m s^{-1}	15–20 m s^{-1}	10–17 m s^{-1}
Gap-flow depth[a]	0.87–1.25 km	0.75–1.13 km	0.37–0.62 km
Gap-jet strength rank	Strongest quartile	Strongest quartile	Middle-two quartiles
Gap-flow-depth rank	Deepest quartile	Deepest quartile	Lowest-two quartiles
Key synoptic characteristics	1) Low-level arctic air mass over the interior 2) Upper-level, negatively tilted ridge over WA/OR coast 3) Upper-level cyclone west of Northern CA	1) Low-level arctic air mass over the interior 2) Upper-level, positively tilted deep trough over WA/OR	1) Low-level arctic air mass over the interior 2) Upper-level strong onshore flow over WA/OR
Weather impacts at the surface	1) 22.7 m s^{-1} gust at PDX (windiest of 406 gust observations for all gap-flow events; study-period max gust: 24.7 m s^{-1}) 2) 17.5 m s^{-1} gust obs at HIO (second windiest of 278 gust obs for all gap-flow events; study-period max gust: 21.6 m s^{-1}) 3) 15.4 m s^{-1} gust at UAO (third windiest of 201 gust obs for all gap-flow events; study-period max gust: 25.7 m s^{-1}) 4) 8.8 m s^{-1} gust at SPB (eighth windiest of 27 gust obs for all gap-flow events; study-period max gust: 19.5 m s^{-1}) 5) 20.1 m s^{-1} gust at TDE (69th windiest of 2195 gust obs for all gap-flow events; study-period max gust: 27.3 m s^{-1})	1) Heaviest snowstorm to affect the Portland area since Dec 2008 caused significant transportation impacts 2) Greatest snow accumulation of 20–40 cm occurred in the western side of Portland 3) 23 cm snow at HIO, SPB 4) 20 cm snow at PDX 5) 10 cm snow at TDE	1) Most impactful freezing-rain event in 20 years caused extended road closures, downed tree limbs, widespread power outages 2) Ice accumulations around Portland as large as 1.25 cm 3) Across the western half of the CRG, 2.5–5.0 cm of ice accumulated 4) Mainly snow fell totaling 30–45 cm over the eastern half of the CRG closest to the cold continental air source

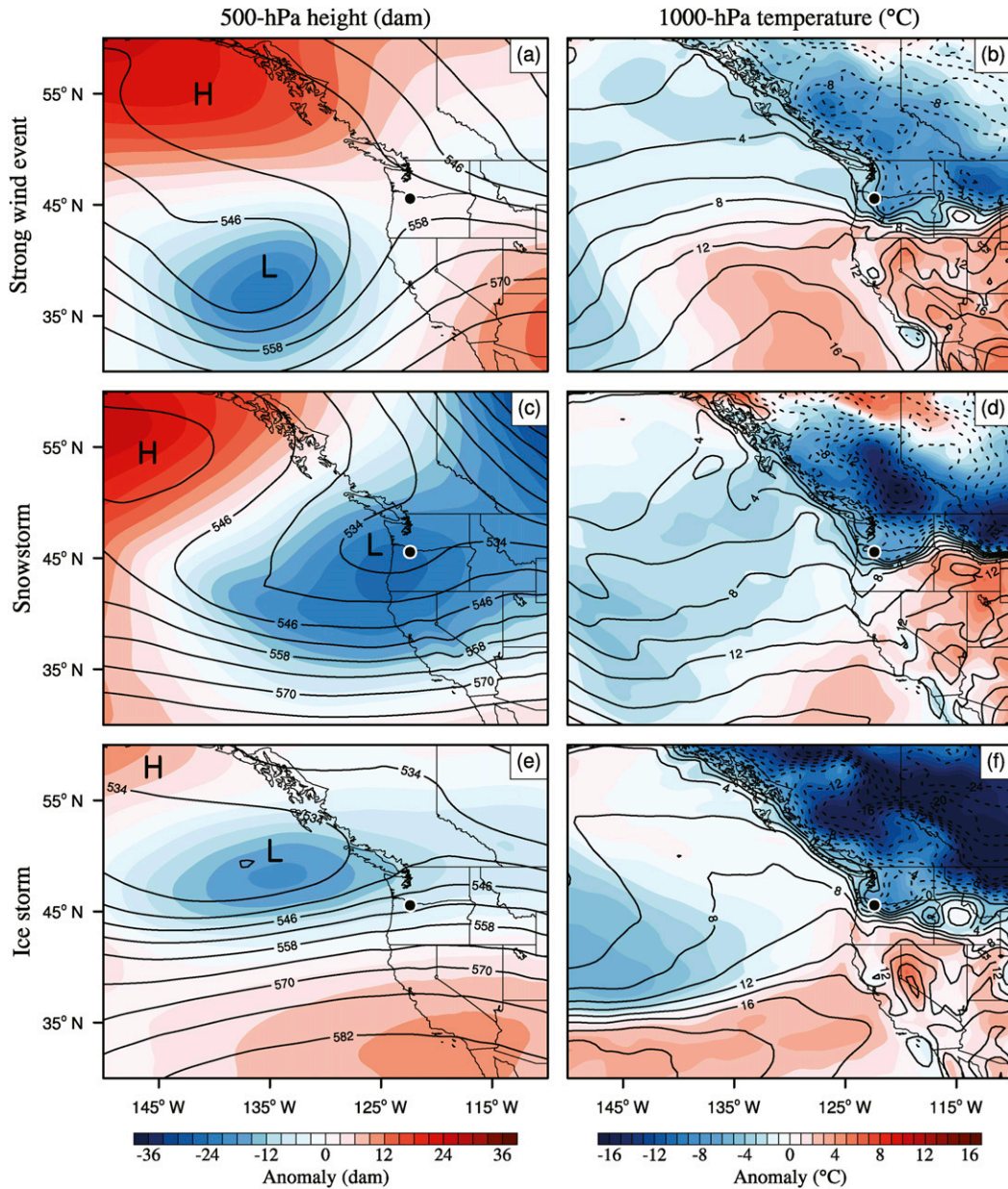[a] Represents the characteristic value ranges observed over a majority (75%) of the time periods listed above.

FIG. 14. Case-composite mean and anomaly analyses (solid and color-filled contours, respectively) for (left) 500-hPa height (dam) and (right) 1000-hPa temperature (°C) derived from NOAA's Climate Forecast System 6-h gridded datasets. (a),(b) Strong wind event, composed of seven 6-h gridded dataset times between 1200 UTC 1 Feb and 0000 UTC 3 Feb 2017. (c),(d) Snowstorm event, composed of three 6-h times between 0600 and 1800 UTC 11 Jan 2017. (e),(f) Ice storm event, composed of six 6-h times between 0000 UTC 9 Dec and 0600 UTC 10 Dec 2016. The anomaly reference period is 1981–2010. The location of TDE is shown with a black dot.

during the first half of the event and the strongest gap-jet speeds occur at midevent. These flow enhancements result from constructive contributions from both frontal-wave and cold-pool forcing, as SLP falls dominate west of the CRG and surface temperatures reach their minimum east of the CRG. During the third phase, gap-flow depth and gap-jet speed decrease during the latter half

of the event, as frontal-wave forcing dominates and cold-pool forcing wanes. Decreasing gap-flow depth coincides with a synoptically driven wind direction shift and subsequent increase in cross-barrier southwesterly flow aloft, which can increase vertical-shear instability and Cascade-leeward effects (e.g., flow acceleration, wave activity, and downslope warming) aloft. The resulting

top-down turbulent mixing warms temperatures within the gap flow at a greater rate to the east than west of the CRG, thus reducing the SLP gradient and flow within the CRG. At the gap exit, snowfall occurs during phases 2 and 3, while freezing rain is confined to phase 3 when the gap flow becomes shallow and cumulative precipitation is maximized prior to cold-frontal passage. In the fourth phase, shallow and relatively weak gap-flow at the western end of the CRG ceases, as the combination of intensifying vertical-shear instability and synoptic-pressure rises occur with cold-frontal passage. During the fifth phase, cold-frontal passage occurs above the cold pool east of the CRG, where the ensuing cold advection aloft can weaken the capping temperature inversion and allow boundary layer mixing to further erode the interior cold pool. The initiation and cessation of the observed gap flows exhibited modest diurnal behavior with the begin (end) times occurring most often during the local evening (morning) hours. We attributed these behaviors to radiational cooling at night and convective turbulent mixing during the day. During the cool season, gap flow was most persistent in January, when longer-duration events associated with an anomalously amplified synoptic-scale pattern were maintained by strong radiational cooling and arctic outbreaks over the interior and warm advection off the coast.

Observations of gap-flow depth and gap-jet strength at the CRG exit served as useful diagnostics for assessing potentially impactful weather, such as wind gusts and winter precipitation, downstream over the Portland metropolitan area. At PDX, HIO, and UAO, where gap-flow spreads horizontally and collapses vertically, gusty surface winds $\geq 7.2\,\mathrm{m\,s}^{-1}$ were associated primarily with the deepest quartile of gap flows at TDE. For the two deepest quartiles, strong gap-jet speed at TDE was also a useful indicator of gusty surface winds across the Portland area and provided value-added information relative to using surface-wind observations at TDE. At TDE and PDX, the number of freezing rain hours mostly increased with decreasing gap-flow depth, while, at the three remaining sites located farther downstream of the CRG, the occurrence of freezing rain was not linked substantively to gap-flow depth. The number of snow reports was directly proportional to the depth of the gap flow. The deepest quartile produced regionally homogenous snow occurrences, whereas the shallowest two quartiles yielded a decrease in freezing-rain occurrences with increasing distance from the CRG. As with surface wind gusts across the Portland area, using gap-jet easterly wind speed instead of the surface-wind counterpart at TDE provided value-added information on winter-type precipitation.

The high-resolution spatiotemporal characteristics of the wind profiler data can also be utilized in numerical-model verification studies to improve forecast performance and process understanding. While a detailed forecast-verification assessment is beyond the scope of this study, a basic assessment was conducted to demonstrate the use of derived observational metrics, namely gap-jet strength and gap-flow depth, as performance measures of the NWS 3-km High-Resolution Rapid Refresh (HRRR; Benjamin et al. 2016) operational forecasts (Fig. 15). The mean difference between observed and forecast gap-jet speed (Fig. 15a) and gap-flow depth (Fig. 15b) show that the forecasts are biased weak and low for all verification times. In particular, the fastest-quartile jets and the deepest-quartile depths are associated with the largest mean errors, which, as demonstrated in section 4, can have significant ramifications on surface wind gust and freezing-precipitation impacts over the Portland metropolitan area. The identification of such errors can help guide future studies to reveal model deficiencies responsible for those errors. For example, the accurate HRRR-forecast results for the shallowest gap-flows in the gap-exit region ($\leq 0.47\,\mathrm{km}$ in Fig. 15b) differ from the case-oriented, model-simulation findings by Sharp (2002), where a 4-km horizontal grid resulted in an elevated gap that prevented cold air from flowing through the CRG. Similar verification analysis could offer evidence-based guidance for these types of model sensitivity studies to more accurately identify the optimum grid resolution for the CRG and also to document the gap-flow-depth-detection limitations of other operational forecast models using coarser grids. In contrast, the degraded forecast performance of the deepest gap flows ($\geq 0.77\,\mathrm{km}$ in Fig. 15b), which should be less sensitive to HRRR misrepresentations in terrain than the shallowest gap-flow-depth cases, suggests that the modeled depth and evolution of the interior cold pool warrants further detailed study.

The observation-based results from this two cool-season study confirm that radar wind profilers provide reliably and continuously detailed wind measurements in all weather conditions that are necessary for studying gap flows. Backscatter from both clear-air below ~1.5 km MSL and frequently occurring precipitation generated above the gap flow in the CRG produced comprehensive time–height data coverage that is unlikely to be matched by other common remote sensing technologies (e.g., lidar and sodar) due to signal attenuation by precipitation. However, because radar clear-air backscatter is dependent on turbulence structures in moisture, decreased performance should be anticipated when attempting to study drier gap flows in higher-elevation terrain or more arid climates using wind profilers.
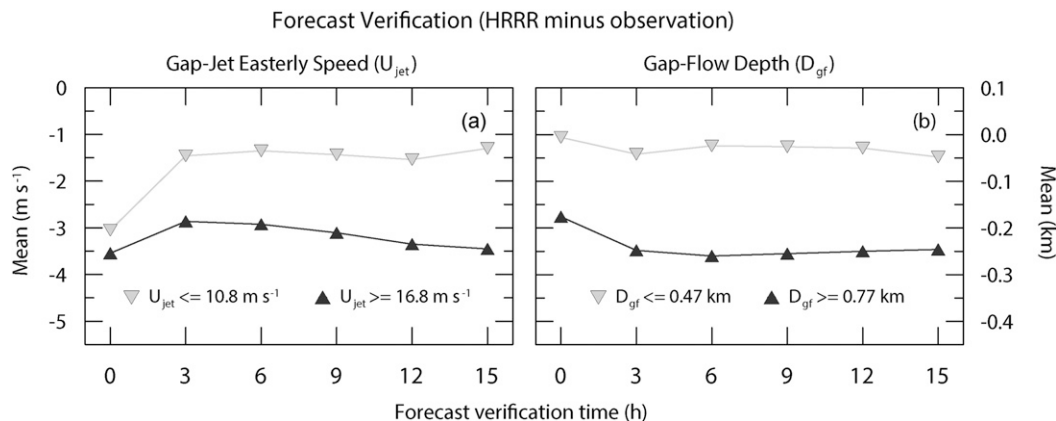
Forecast Verification (HRRR minus observation)

FIG. 15. Forecast verification statistics based on differences between hourly TDE wind profiler observations and HRRR (i.e., HRRR minus observations) for the observed top and bottom quartiles (black and gray triangles, respectively) of (a) mean gap-jet easterly wind speed (m s^{-1}) and (b) mean gap-flow depth (km MSL). The top- and bottom-quartile thresholds for gap-jet speed are 16.8 and 10.8 m s^{-1}, respectively, and for gap-flow depth are 0.77 and 0.47 km MSL, respectively. Forecast verification times are at 3-h intervals, from the initialization through 15 h. The observed and modeled hourly gap-jet speed and gap-flow depth are determined using the automated algorithm in Neiman et al. (2018).

Despite the comprehensive kinematic depiction provided by the radar wind profiler in this study, significant deficiencies remain in acquiring and resolving the vertical temperature structure. The height coverage of the RASS measurements at TDE was <0.5 km MSL during the windiest gap flows, with a maximum height coverage of 1.5 km MSL during the weakest flow regimes. The strongest and deepest wind composite analyses at WCO (Figs. 3, 4) suggest that the cold-air reservoir located east of the CRG is at least as deep as 1.25 km MSL. As such, further observational and modeling-verification studies of the interior cold pool depth and evolution will require improvements in the vertical temperature measurement. Furthermore, the physical processes responsible for the rapid changes in gap-flow depth and gap-jet speed along the CRG may be associated with thermodynamic changes well above the gap-flow (e.g., related to mountain wave activity), and may require vertical temperature profiling up to midtropospheric levels (Mayr et al. 2007). In an attempt to address this measurement shortcoming, ESRL is activity pursuing alternative RASS sampling methods, including the use of acoustic sources at multiple radii from the radar antenna, to improve height coverage during windy periods. Experimentation is also underway to augment ground-based microwave-radiometer calibrations with real-time, low-level RASS temperature profiles, which may offer the greatest potential for detailed temperature profiling up to the midtropospheric altitudes.

Last, the continuous spatiotemporal quality of the results in this study verify that the objective-analysis methodologies of Neiman et al. (2018) are likely applicable to other observational and modeling investigations of gap flow, with comparable data resolutions (i.e., a minimum of hourly vertical profiles with 60-m resolution). In addition, there is potential to use additional metrics for the future study of gap flows. For example, if temperature-profiling improvements are realized, the bulk vertical gradients of horizontal velocity and temperature can be used (via the Bulk Richardson Number) to estimate the presence and magnitude of turbulence at the top of and within gap flows. Such data could be used to explore whether turbulent mixing at the top of gap flows plays a significant role in their cessation, which could be corroborated further by enhanced spectral-width measurements in the radar Doppler spectrum during clear-air backscatter (e.g., White et al. 1999; McCaffrey et al. 2017). Also, during clear-air return, there is potential to detect vertical velocity associated with mesoscale processes, such as mountain waves, that may contribute to the rapid along-gap modulation of gap-flow depth that has been observed in this and prior studies.

REFERENCES

Benjamin, S. G., and Coauthors, 2016: A North American hourly assimilation and model forecast cycle: The Rapid Refresh. *Mon. Wea. Rev.*, **144**, 1669–1694, https://doi.org/10.1175/MWR-D-15-0242.1.

Bond, N. A., C. F. Dierking, and J. D. Doyle, 2006: Research aircraft and wind profiler observations in Gastineau channel during a Taku wind event. *Wea. Forecasting*, **21**, 489–501, https://doi.org/10.1175/WAF932.1.

Carter, D. A., K. S. Gage, W. L. Ecklund, W. M. Angevine, P. E. Johnston, A. C. Riddle, J. S. Wilson, and C. R. Williams, 1995: Developments in UHF lower tropospheric wind profiling at NOAA's Aeronomy Laboratory. *Radio Sci.*, **30**, 977–1001, https://doi.org/10.1029/95RS00649.

Colle, B. A., and C. F. Mass, 2000: High-resolution observations and numerical simulations of easterly gap flow through the Strait of Juan de Fuca on 9–10 December 1995. *Mon. Wea. Rev.*, **128**, 2398–2422, https://doi.org/10.1175/1520-0493(2000)128<2398:HROANS>2.0.CO;2.

Finn, D., and Coauthors, 2016: Evidence for gap flows in the Birch Creek Valley, Idaho. *J. Atmos. Sci.*, **73**, 4873–4894, https://doi.org/10.1175/JAS-D-16-0052.1.

Gaberšek, S., and D. Durran, 2006: Gap flows through idealized topography. Part II: Effects of rotation and surface friction. *J. Atmos. Sci.*, **63**, 2720–2739, https://doi.org/10.1175/JAS3786.1.

Green, M. C., J. Xu, and N. Adhikari, 2008: Transport of atmospheric aerosol by gap winds in the Columbia River Gorge. *J. Appl. Meteor. Climatol.*, **47**, 15–26, https://doi.org/10.1175/2007JAMC1561.1.

Martner, B. E., and Coauthors, 1993: An evaluation of wind profiler, RASS, and microwave radiometer performance. *Bull. Amer. Meteor. Soc.*, **74**, 599–613, https://doi.org/10.1175/1520-0477(1993)074<0599:AEOWPR>2.0.CO;2.

Mayr, G. J., and Coauthors, 2004: Gap flow measurements during the Mesoscale Alpine Programme. *Meteor. Atmos. Phys.*, **86**, 99–119, https://doi.org/10.1007/s00703-003-0022-2.

——, and Coauthors, 2007: Gap flows: Results from the mesoscale Alpine programme. *Quart. J. Roy. Meteor. Soc.*, **133**, 881–896, https://doi.org/10.1002/qj.66.

McCaffrey, K., L. Bianco, and J. M. Wilczak, 2017: Improved observations of turbulence dissipation rates from wind profiling radars. *Atmos. Meas. Tech.*, **10**, 2595–2611, https://doi.org/10.5194/amt-10-2595-2017.

McDonald, A. J., T. K. Carey-Smith, D. A. Hooper, G. J. Fraser, and B. P. Lublow, 2004: The effect of precipitation on wind-profiler clear air returns. *Ann. Geophys.*, **22**, 3959–3970, https://doi.org/10.5194/angeo-22-3959-2004.

Neiman, P. J., F. M. Ralph, A. B. White, D. D. Parrish, J. S. Holloway, and D. L. Bartels, 2006: A multiwinter analysis of channeled flow through a prominent gap along the northern California Coast during CALJET and PACJET. *Mon. Wea. Rev.*, **134**, 1815–1841, https://doi.org/10.1175/MWR3148.1.

——, D. J. Gottas, A. B. White, W. R. Schneider, and D. Bright, 2018: A real-time online data product that automatically detects easterly gap flow events and precipitation type in the Columbia River Gorge. *J. Atmos. Oceanic Technol.*, **35**, 2037–2052, https://doi.org/10.1175/JTECH-D-18-0088.1.

Saha, S., and Coauthors, 2010: The NCEP Climate Forecast System Reanalysis. *Bull. Amer. Meteor. Soc.*, **91**, 1015–1057, https://doi.org/10.1175/2010BAMS3001.1.

——, and Coauthors, 2014: The NCEP Climate Forecast System version 2. *J. Climate*, **27**, 2185–2208, https://doi.org/10.1175/JCLI-D-12-00823.1.

Sharp, J. M., 2002: Columbia Gorge gap flow: Insights from observational analysis and ultra-high-resolution simulation. *Bull. Amer. Meteor. Soc.*, **83**, 1757–1762, https://doi.org/10.1175/BAMS-83-12-1757.

——, 2005: The structure and dynamics of Columbia Gorge gap flow revealed by high-resolution numerical modeling. Ph.D. thesis, University of Washington, 190 pp.

——, and C. F. Mass, 2004: Columbia Gorge gap winds: Their climatological influence and synoptic evolution. *Wea. Forecasting*, **19**, 970–992, https://doi.org/10.1175/826.1.

White, A. B., R. J. Lataitis, and R. S. Lawrence, 1999: Space and time filtering of remotely sensed velocity turbulence. *J. Atmos. Oceanic Technol.*, **16**, 1967–1972, https://doi.org/10.1175/1520-0426(1999)016<1967:SATFOR>2.0.CO;2.

——, and Coauthors, 2013: A twenty-first-century California observing network for monitoring extreme weather events. *J. Atmos. Oceanic Technol.*, **30**, 1585–1603, https://doi.org/10.1175/JTECH-D-12-00217.1.

Whiteman, C. D., S. Zhong, W. J. Shaw, J. M. Hubbe, and X. Bian, 2001: Cold pools in the Columbia Basin. *Wea. Forecasting*, **16**, 432–447, https://doi.org/10.1175/1520-0434(2001)016<0432:CPITCB>2.0.CO;2.

Wilczak, J. M., and Coauthors, 2019: The second Wind Forecast Improvement Project (WFIP2): Observational field campaign. *Bull. Amer. Meteor. Soc.*, **100**, 1701–1723, https://doi.org/10.1175/BAMS-D-18-0035.1.

Zhong, S., C. D. Whiteman, X. Bian, W. J. Shaw, and J. M. Hubbe, 2001: Meteorological processes affecting the evolution of a wintertime cold air pool in the Columbia Basin. *Mon. Wea. Rev.*, **129**, 2600–2613, https://doi.org/10.1175/1520-0493(2001)129<2600:MPATEO>2.0.CO;2.